JOURNAL OF GEOPHYSICAL RESEARCH, VOL. 104, NO. A1, PAGES 115-141, JANUARY 1, 1999

Atmospheric holes: Instrumental and geophysical effects

L. A. Frank and J. B. Sigwarth

Department of Physics and Astronomy, University of Iowa, Iowa City

Abstract. Global images of far-ultraviolet dayglow with the Earth Camera on board the Polar spacecraft were used for a comprehensive study of transient, localized decreases of intensities, also known as atmospheric holes. An automated determination for detection of an atmospheric hole was developed and employed in this survey of the characteristics of this phenomenon, which avoided the possibility of aliasing by visual inspection of the images. An extensive investigation of possible instrumental effects included (1) evaluation of random rates for a period in mid-January for which there were no atmospheric holes, thus providing an excellent inflight calibration of the instrument's noise, (2) the effects in the images due to energetic electrons in the outer radiation zone, (3) the nonuniform sensitivities for the pixels of the sensor, or "hot spots," and (4) the contributions of longer wavelength radiation from the atmosphere to the camera's responses. For the straightforward selection criteria for the identification of atmospheric holes the instrumental effects were not major contributors to the occurrence frequencies of this phenomenon. The subsequent search for geophysical effects revealed (1) a strong altitude dependence of the frequency of atmospheric holes, (2) a substantial local-time variation of rates which favored locations in the local-morning sectors of the atmosphere relative to those in the evening, (3) increasing sizes of the atmospheric holes as the spacecraft altitude decreases, and (4) large seasonal variations in the hole rates during the period November 1997 through late January 1998 which were remarkably similar to those observed during the same months but 16 years earlier with Dynamics Explorer 1.

1. Introduction

Transient decreases of Earth's far-ultraviolet dayglow were first detected with a spin-scan imager on board the Dynamics Explorer 1 spacecraft which was launched into an eccentric polar orbit for global views of the auroral zones and dayglow. The diameters of these transient decreases, or atmospheric holes, were in the range of 50 to 100 km, and their durations were about 100 s [*Frank et al.*, 1986a]. Because the dimensions of the atmospheric holes were large, this phenomenon was interpreted as water vapor clouds from small comets which were disrupted and vaporized by sunlight above the upper atmosphere [*Frank et al.*, 1986b]. Water vapor is an efficient absorber of the far-ultraviolet emissions, primarily those from atomic oxygen at 130.4 and 135.6 nm, from the upper atmosphere.

Several years of intensive examination of these images prior to publication found that some features of the atmospheric holes could not be accounted for by an instrument artifact. These are summarized by *Frank and Sigwarth* [1993] as (1) preferential motion in the east-to-west direction across the sunlit face of Earth, (2) larger angular diameters for these atmospheric holes when the spacecraft approached its lowest orbital altitudes, (3) similar diurnal variations in occurrence rates as those for radar meteors, and (4) correlation of the occurrence rates with the nonshower meteors as monitored with forward scatter radar. However, because of the startling implications of the large individual masses of these small comets, tens of tons, and the infall rate into our atmosphere of about 10 million per year, the overwhelming majority of the scientific community was convinced that the atmospheric holes were merely an instrument artifact [*Dessler*, 1991].

A set of three state-of-the-art cameras was recently launched into a high-altitude, eccentric polar orbit and provides marvelous views of Earth's aurora and far-ultraviolet dayglow. The designs of these three cameras, two cameras for visible light and the third for ultraviolet emissions, on board the Polar spacecraft were greatly dissimilar to those previously flown on the Dynamics Explorer 1 spacecraft [*Frank et al.*, 1981, 1995]. The three cameras on the Polar spacecraft are known as the Visible Imaging System (VIS) and are capable of far greater spatial and temporal resolutions relative to those for Dynamics Explorer 1. These new observations with the Polar spacecraft have confirmed the occurrence rates, dimensions, and east-to-west motions of atmospheric holes [*Frank and Sigwarth*, 1997a]. The ability to image the atmospheric holes in two consecutive frames has also confirmed that the diameters of the holes are increasing at the rate of about 1 km/s, as expected for the vaporization of the water snows in the disrupted body of a small comet. The cluster of darkened pixels in the images of the atmospheric holes confirms that the amount of water in a small comet is typically in the range of tens of tons. There is a companion camera, the UVI, on board the Polar spacecraft which is also capable of observing the

Paper number 1998JA900011.
0148-0227/99/1998JA900011$09.00

atmospheric far-ultraviolet dayglow [*Torr et al.*, 1995]. However, the spatial resolution of this camera is insufficient to use for the detection of atmospheric holes except for an extremely limited data set of less than 2 hours in duration. Analysis of this limited data set showed that the atmospheric holes are simultaneously detected at the same position in the dayglow as independently viewed with the two cameras [*Frank and Sigwarth*, 1997b]. These simultaneous sightings were not coincidental because during a 64-minute interval on April 12 only 10 holes were observed in 116 VIS images and 11 holes in 53 UVI images. Only two sets of simultaneous sightings were available due to the nonsynchronous timings of the frames from the two cameras. For these two sets of frames, the holes were sighted at the same position in the dayglow with the two cameras.

An unexpected supporting observation of the existence of a heretofore undiscovered population of interplanetary objects was the occurrence of bright atomic oxygen trails at 130.4 nm when a few of the small comets disrupt at very high altitudes, 10,000 km or more, above the Earth's surface [*Frank and Sigwarth*, 1997c]. These occasional disruptions are sufficiently high to separate the comet trail from the intense atmospheric dayglow.

Recently, one of the two visible cameras in the VIS complement was employed to independently determine the typical mass of water in a small comet by imaging the OH emissions at 308.5 nm, which is the standard proxy for determining the mass of water vapor for the well-known large comets [*Frank and Sigwarth*, 1997d]. Three consecutive images of each water cloud were taken. This independent determination of the mass of a small comet is tens of tons and equal to that inferred from the sizes of atmospheric holes. The occurrence rate of the OH trails was very similar to that for atmospheric holes, thus providing observational closure on the source of the atmospheric holes.

Even so, the interpretation of the atmospheric holes as due to small comets remains controversial because of the unsettling implications. The present paper concentrates on the new observational evidence for the existence of atmospheric holes.

We report here a comprehensive investigation of the observations of atmospheric holes with the Earth Camera on board the Polar spacecraft. Section 2 provides an overview of recent papers offering criticisms of the existence of atmospheric holes. Section 3 is directed toward instrumental effects and the criteria for an automated detection of atmospheric holes. Section 4 reports the geophysical effects which were found with the automated search. A summary and discussion of several of the important findings may be found in section 5.

2. Criticisms of the Existence of Atmospheric Holes

Several papers have been recently accepted for publication which conclude that the atmospheric holes in the VIS Earth Camera images are due to instrumental artifacts. Such publications provide a useful forum for the discussion of this controversial topic. We summarize here the major criticisms which are offered by these papers.

The results of a search for atmospheric holes with the other far-ultraviolet camera, the UVI, on board the Polar spacecraft were reported by *Parks et al.* [1997]. These authors concluded that there was no corroboration of the atmospheric holes in their data on the basis that (1) the occurrence frequencies of darkened pixel clusters as a function of the number of pixels in a cluster was a featureless distribution with no evidence of any contribution other than that from sensor noise, (2) there was no evidence of the wobble of the spacecraft platform on which the camera is mounted, and (3) there was no evidence of the bright oxygen trails in the dark sky beyond Earth's limb. A second, similar paper by *Parks et al.* [1998] includes additional observations from the VIS Earth Camera for April 12 and September 23, 1996.

Mozer et al. [1998] present an analysis of a preliminary working catalog of atmospheric hole events at the University of Iowa web site www-pi.physics.uiowa.edu wwwvis/, which has been subsequently updated with improved search criteria. *Mozer et al.* [1998] also claim that there is no feature in the occurrence frequency of darkened pixel clusters as a function of numbers of pixels which would indicate that atmospheric holes are a geophysical reality. The remaining criticism stated by *Mozer et al.* [1998] is that no altitude dependence of the sizes of atmospheric holes is found in the VIS Earth Camera images.

McFadden et al. [1998] report the results of their calculations of the expected distributions of clusters of darkened pixels on the basis of the characteristics of one element of the Earth Camera sensor, i.e., the microchannel plate. By adjusting the width of the Gaussian distribution of pixel intensities at the phosphor plate which follows the microchannel plate, these authors are able to generate a distribution of darkened clusters which is in the range of those observed by the Earth Camera. They use the same set of atmospheric hole detections which are based upon search criteria employed by *Mozer et al.* [1998]. *McFadden et al.* [1998] claim that nonuniformities in the pixel sensitivities of the sensor will not give false hole detections for their chosen criteria of $-2.0\ \sigma$. These authors claim that most of the atmospheric holes are due to the effects of energetic particles penetrating into the sensor of the Earth Camera.

The baseline criticism adopted in all of the above four papers is that there is no distinguishing feature in the occurrence rates of darkened pixel clusters as a function of the numbers of pixels in the cluster. Indeed, robust features in the occurrence frequencies which are associated with the presence of atmospheric holes as geophysical events are observed with both cameras on the Dynamics Explorer 1 and the Polar spacecraft. These features are the subject of the present paper.

3. Instrumental Effects

3.1. Overview of the Instrumentation

On February 24, 1996, the Polar spacecraft was launched into an eccentric orbit with perigee and apogee altitudes of 5170 and 50,510 km, respectively, an inclination of 86°, and an orbital period of 17.6 hours. The apogee position was located at 68°N. The Earth Camera

was mounted on a despun platform in order to provide staring at far-ultraviolet features of the auroras and the dayglow and thus to gain greatly enhanced sensitivity relative to that for viewing from the spinning body of the spacecraft. A detailed description of this camera is given by *Frank et al.* [1995].

For the present paper it is worthwhile to note that the field of view of the Earth Camera is 20° × 20° and is serviced by a charge-coupled device (CCD) which provides coverage with an array of 256 × 256 individual picture elements (pixels) with angular dimensions of 0.08° × 0.08°. After launch it was found that the spacecraft center of mass could not be positioned on the spin axis of the spacecraft. The platform then executes a cyclic motion which, as seen by the cameras, has an amplitude of 0.38° and a period of 6 s, the rotation period of the main spacecraft body. This large-amplitude motion was unacceptably degrading for the angular resolution of the Earth Camera and was eliminated with the use of the onboard instrument computers, the electronic shutter, and the spacecraft timing and aspect signals soon after launch [*Frank and Sigwarth,* 1997a]. All images used in the present paper were acquired in this instrument operating mode. The filter passband is 124–149 nm for which the most prominent dayglow emission is that from atomic oxygen at 130.4 nm. For the present series of observations the acquisition time for the images is 33 s, including the time for shutter closure. The repetition rate for image acquisition varied with the operating mode of the instrument.

As previously discussed by *Frank and Sigwarth* [1997c], the cyclic platform motion which degrades the angular resolution of the Earth Camera is compensated for by electronically shuttering the camera in synchronization with the spacecraft spin. The projection of the platform motion onto the sky provides two ansas for which the viewing time as a function of platform direction is a maximum. The electronic shuttering allows only one of these ansas to be recorded by the camera. Also, the shuttering is used to exclude periods for which the large antennas come into view of the camera so that scattered light is not recorded in the images. On April 28, 1996, the Earth Camera was commanded into a mode to compensate for the platform motion. The angular sectors for which the shutter was open were 87.2° to 17.6° as the spacecraft rotates toward the selected ansa and 2.8° to 72.4° after the spacecraft rotation passes the ansa. The corresponding pixel resolution for viewing a star is improved to 2.2 pixels relative to the 4.8 pixels without compensation. On November 7, 1996, the shutter timings were slightly adjusted to improve the angular resolution to 1.6 pixels. The corresponding angular sectors were 70.3° to 17.6° and 2.8° to 70.3°. This angular resolution is equal to the full width at half maximum of the camera's point spread function as determined by viewing stars.

An example of an atmospheric hole is shown in the left-hand panel of Plate 1. This image of the far-ultraviolet dayglow was acquired at 2026 UT on June 10, 1997, from the spacecraft position at an altitude 25,860 km and geographic latitude and longitude of 34.6°N and 178.9°E, respectively. For reference a coastline map has been placed onto the image in the right-hand panel of Plate 1. The somewhat darker linear feature across the dayglow in Plate 1 is due to a decrease in the sensitivity of the image tube from the manufacturing process. This is a raw image with no interpolation between the pixels. The only processing of this image is the removal of small bright clusters of pixels due to penetrating charged particles with the algorithm discussed below. Statistical fluctuations in the sensor responses can be seen in the image. There are only two clusters of darkened pixels which are identified as atmospheric holes, one of which is indicated in Plate 1, with the automated search algorithm described in the next subsection. The purpose of this section of the paper is a detailed discussion of instrumental effects on the observations of atmospheric holes such as that identified in Plate 1.

3.2. Parameters for the Automated Survey for Atmospheric Holes

Our initial detection of atmospheric holes in the Earth Camera images was accomplished by determining the mean pixel responses and the standard deviation of the pixel responses in the vicinity of visually identified clusters of darkened pixels [*Frank and Sigwarth,* 1997a]. The decreases of responses for each pixel in the darkened cluster were then computed in terms of the number of standard deviations, and then statistical tables for Gaussian distributions were employed for determining the probability of occurrence for the darkened cluster. Although this method of determining the statistical robustness of a darkened pixel cluster is valid, it does not provide a basis for the automated survey of atmospheric holes in a large data base.

An atmospheric hole is defined as a cluster of five or more contiguous darkened pixels, each pixel with a decrease in pixel responses of $\leq -M$ standard deviations (σ) below the mean responses. The operation of the computer software is straightforward. A block of 7 × 7 pixels is centered on the pixel to be tested. The mean and standard deviation for evaluating this pixel are computed from the 32 pixels along the perimeter of this pixel block. An inventory of all pixels with responses $\leq -M\sigma$ is acquired. The inventory is then searched for the occurrence of clusters with a given pixel population. In order to achieve hole detections which are robust to the charge depositions due to penetrating energetic charged particles in the radiation zones a lower limit on the value of a standard deviation is chosen. For our searches this value of σ is chosen to be 7.5 DN (DN, digitization numbers) for all pixels in an atmospheric hole, a value which is effective in eliminating false hole detections due to the radiation backgrounds. The reader should note that the search criteria are simple and minimized with regards to the number of free parameters.

A value for M, the number of standard deviations, must be selected. A possible choice is M = 2. The normalized frequency of darkened clusters with $\geq$ N pixels as a function of the number of pixels in a cluster is shown in Figure 1 for a series of images acquired on June 1, 1997. In the later section for geophysical effects a strong local time dependence of atmospheric hole rates in the atmosphere is identified. Hence a sector of at-

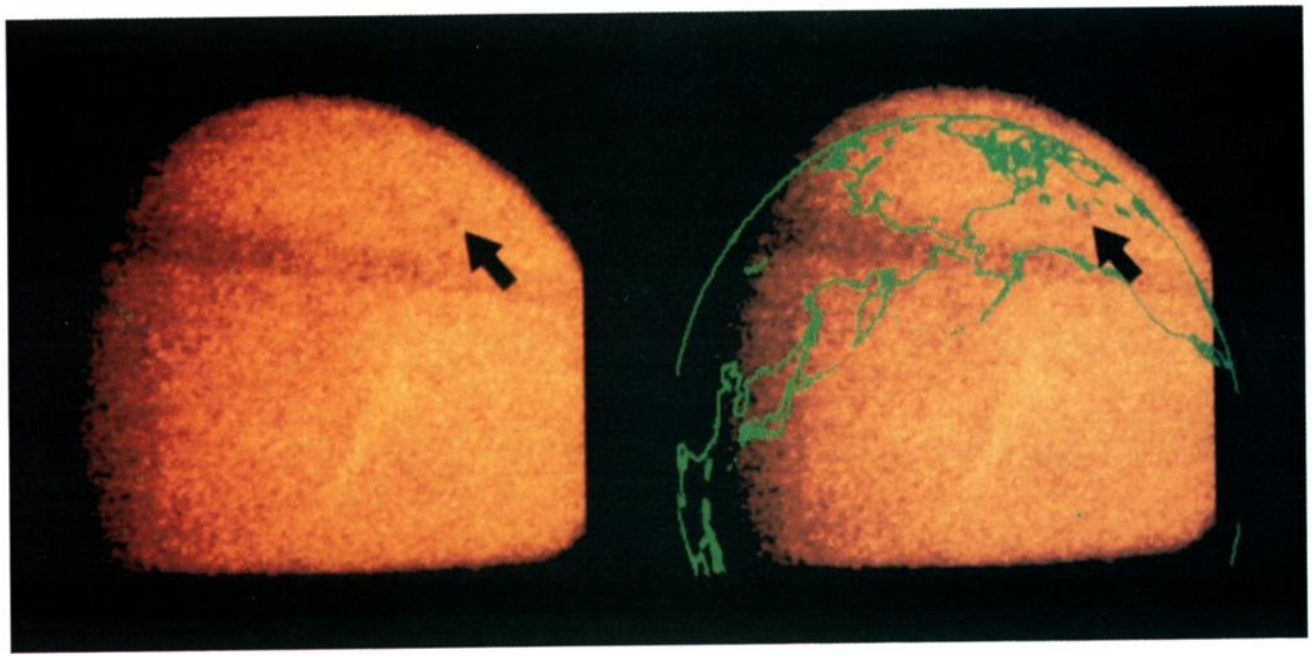

Plate 1. In the left–hand panel is shown a global image of the far–ultraviolet emissions from the upper atmosphere which was acquired with the Earth Camera on board the Polar spacecraft at 2026 UT on June 10, 1997. A coastline map has been superposed on this image in the right–hand panel. Note the localized decrease of dayglow intensities which is called an "atmospheric hole." The event occurred near the southern shore of Lake Athabaska in northwest Saskatchewan, Canada.

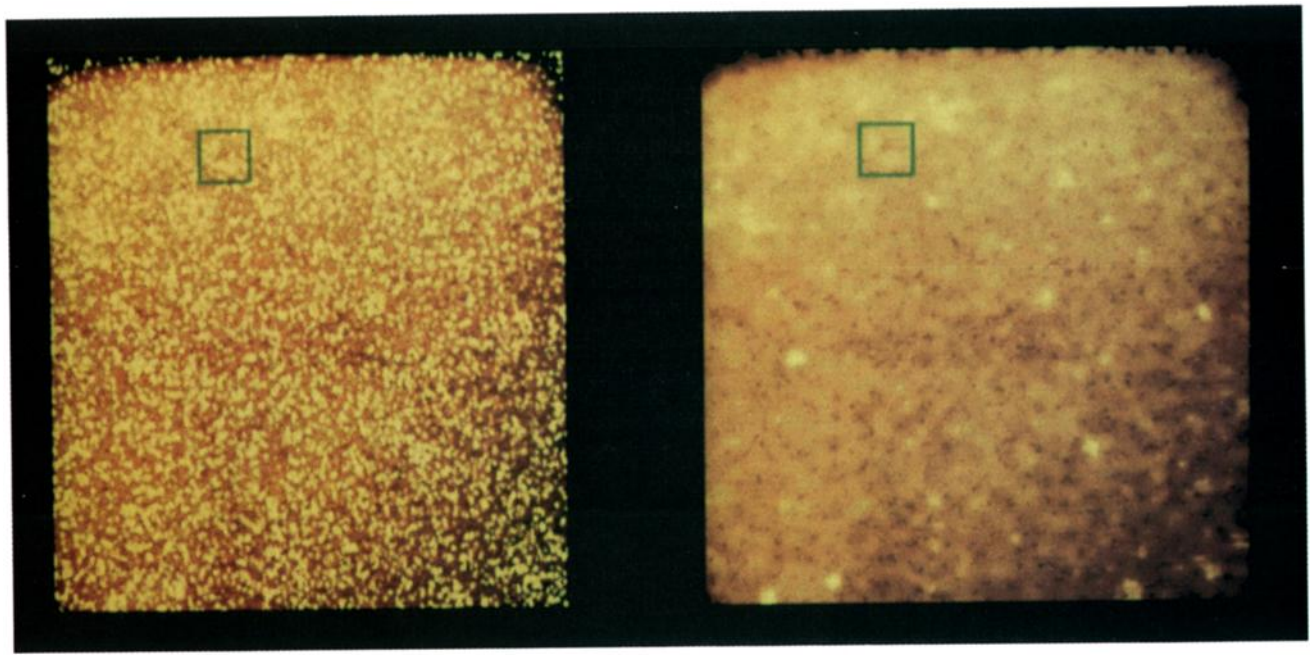

Plate 2. A worst–case example of the effects of penetrating electrons from the radiation zone into the sensor of the Earth Camera: (left) the raw image and (right) the same image after a simple algorithm is used to reduce the amplitudes of the pixel response increases due to the penetrating particles. The box shows an example of an atmospheric hole which was identified with the automated hole detection algorithm. Careful inspection of this hole in both images finds that the hole is preserved even though there is a substantial fraction of the image which is unusable due to the penetrating radiation. On the other hand, a substantial fraction of false detections were identified by the automated search. This image is not usable for determination of hole rates. This image was taken at 2138:16 UT on November 25, 1997, at spacecraft altitude, latitude, and longitude of 17,937 km, 26.1°N and 169.2°E, respectively.

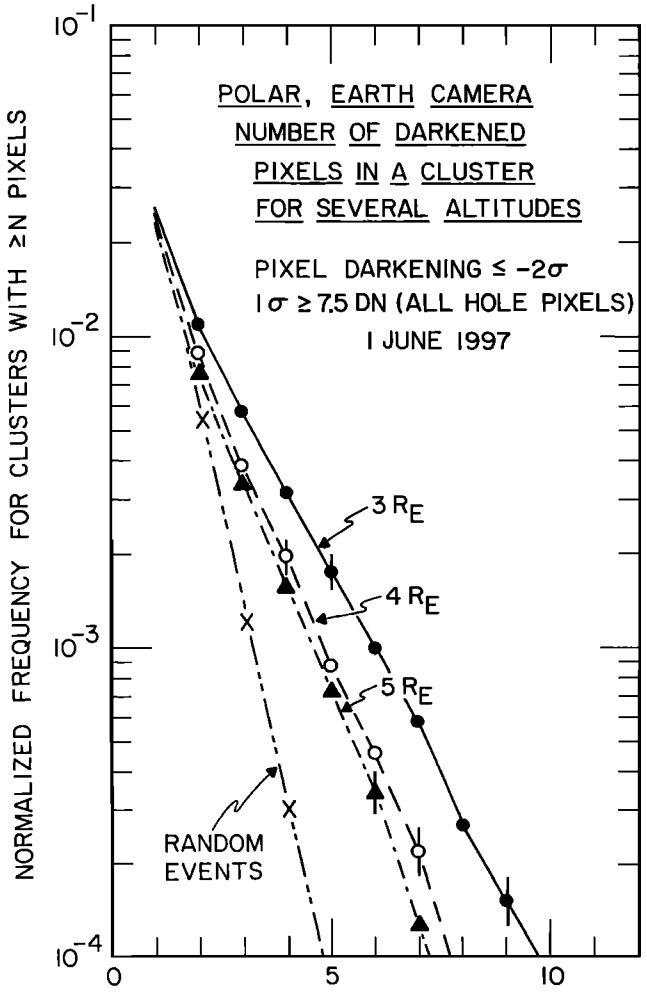

Figure 1. The normalized frequency of darkened pixel clusters as a function of the number of pixels in the cluster for June 1, 1997. These frequencies are shown for three altitude bins and decrease with increasing altitude. The random rates are also shown. The requirements for detection of a cluster is a membership of 5 or more pixels with response decreases of ≤ −2.0 σ and a standard deviation of ≥ 7.5 DN.

mospheric dayglow must be selected in order to properly determine the atmospheric hole rates for the three altitude bins of Figure 1. The dayglow area which was selected is bounded by corner coordinates (14.5°, −52.5°), (30.0°, −52.5°), (30.0°, −22.5°), (14.5°, −22.5°). The center for these Earth-centered solar ecliptic coordinates is at the subsolar point (0°,0°). The hole event rate shown in Figure 1 decreases with increasing altitude as expected for viewing geophysical events in the atmosphere. This decrease is due to the fact that the dimensions of the holes are sufficiently small that many are not detected at the higher altitudes as their dimensions decrease below the pixel resolution of the camera.

The random rate for the occurrence of atmospheric holes is also shown in Figure 1. This random rate is computed from the well-determined characteristics of the sensor of the Earth Camera. The detailed description of the calculation of random rates is given in section 3.7 which follows the analyses of all of the known instrumental effects which might lead to false identification of atmospheric holes. The simulation of the instrument responses for the random rates includes the Poisson distribution of events at the photocathode, the point spread function for charges arriving at the input face of the microchannel plates, and the Gaussian spread of charge amplitudes by the multiplication process in the microchannel plates, the phosphor responses and the CCD noise. The simulated images are processed with the same hole-seeking code as employed for the actual images. The determination of the random rates is validated by comparison with inflight calibration images for which no atmospheric holes are present (section 3.3). The random rates shown in Figure 1 would appear to be significantly less than the observed rates. As is shown in the following analyses of instrumental effects, the value M = 2 is insufficient to exclude a substantial fraction of false events. A larger value of M must be chosen in order to assure the robustness of the automated search for atmospheric holes.

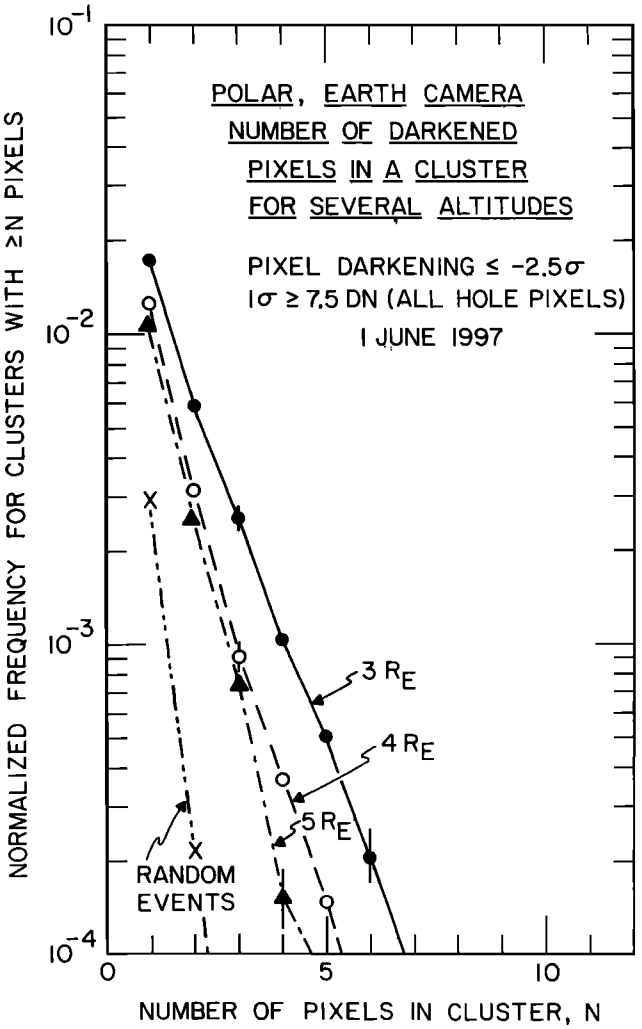

Figure 2. Same plot as Figure 2 except that the hole detection criteria have been changed to a decrease in pixel responses ≤ −2.5 σ. Again, the standard deviation is ≥ 7.5 DN. These are the criteria employed for the automated atmospheric hole survey reported in this paper. Note that the random event rates are insignificant relative to the observed rates for all three altitude bins.

In order to achieve a robust, automated determination of the actual hole rates the required darkening per pixel is increased to M = 2.5. Unless otherwise noted this value is used throughout our presentation with a minimum σ of 7.5 DN. The results are shown in Figure 2. The random rate is insignificant relative to the observed hole rates for the three spacecraft altitude bins.

3.3. Verification of the Accuracy of the Random Event Rates

Because of the untimely failure of the sensor and electronics of the Earth Camera during the instrument testing in a thermal–vacuum chamber at the Goddard Space Flight Center the tight schedule for the repair activities precluded the acquisition of a series of images for uniform exposure with an external light source. Hence a determination of the random atmospheric hole rate in the laboratory was not possible. In any case, the laboratory conditions would not have exactly duplicated those in spaceflight because of the temperature gradients due to the instrument radiators and because of the extensive adjustments of sensor operating voltages and gain settings relative to those employed in the laboratory. Still, it would have been helpful to have such laboratory measurements. Except for the photocathode material the two sensors for the cameras at visible wavelengths are identical to the sensor in the Earth Camera. These sensors for the visible cameras did not exhibit clusters of dark pixels in the laboratory and inflight data which

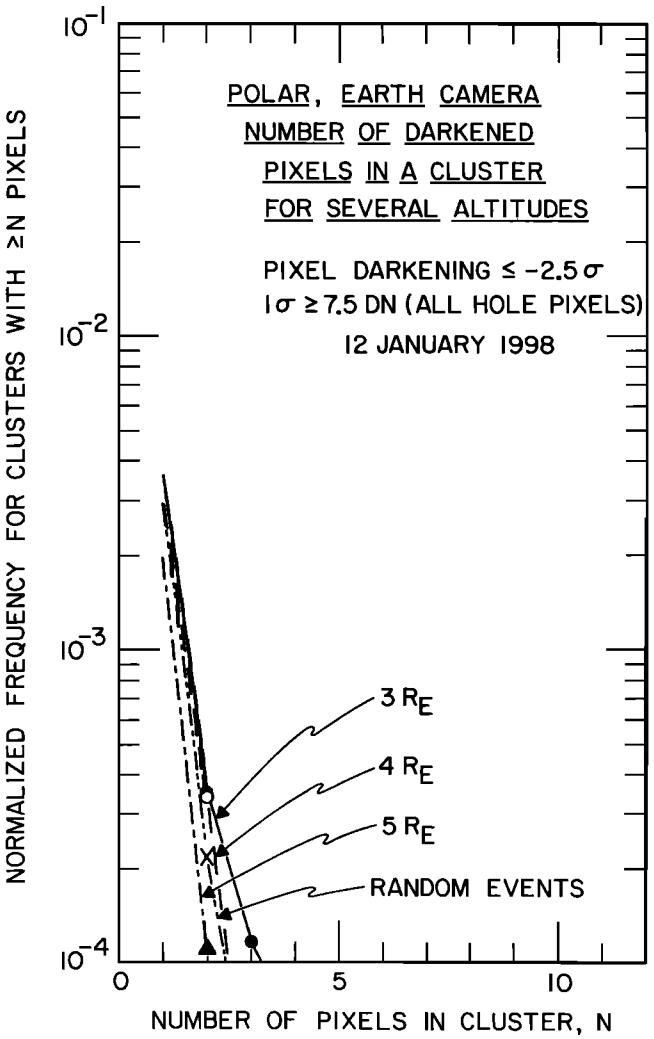

Figure 3. Normalized frequency of darkened pixel clusters as a function of numbers of pixels in the cluster for January 12, 1998, in the same format as Figures 1 and 2. These data are taken during the mid-January minimum in atmospheric hole rates. No holes are detected during this day and provide an inflight verification of the calculation of random rates and, more importantly, a series of "laboratory" images for which the darkened pixel clusters corresponding to atmospheric holes do not appear.

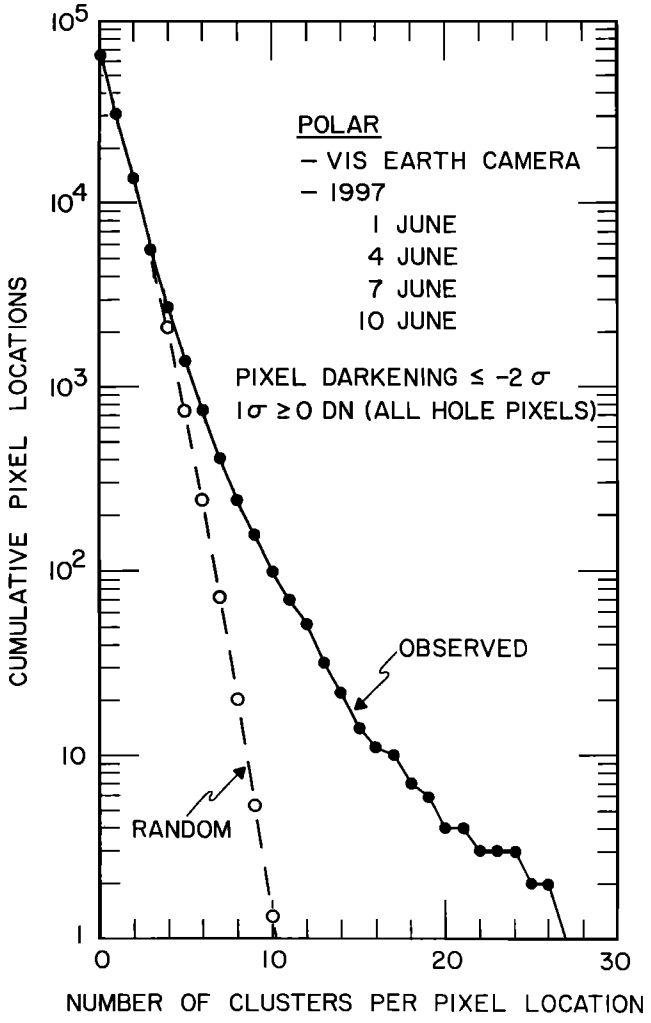

Figure 4. Survey of "hot spots" in the Earth Camera sensor by plotting the cumulative pixel locations as a function of the number of darkened clusters per pixel location for images taken during June 1, 4, 7, and 10, 1997. For example, about 100 pixels were characterized by the occurrence of 10 or more clusters. A dark pixel cluster is defined as 5 or more contiguous pixels, each with reduced responses of ≤ −2.0 σ. No restrictions are placed upon the values of the standard deviations. The observed distribution departs greatly from a random distribution of events in the sensor pixels. This means that the effects of variations in the sensitivity of the pixels influence the event rate of clusters to an unacceptable extent.

would mimic the atmospheric holes seen in the flight data for the Earth Camera.

It is very fortunate that there is a short period in mid-January during which no atmospheric holes are detected with the Earth Camera. This seasonal feature of the hole rates was previously observed with the spin-scan ultraviolet photometer on board Dynamics Explorer 1 [*Frank and Sigwarth*, 1993]. These observations with the Polar Earth Camera for January 12, 1998, are shown in Figure 3. The normalized frequency of clusters with ≥ N pixels as a function of N is shown for three altitude bins. As expected, the hole rates coincide with the random rates for all three altitude bins. Thus our computations of the random rates are verified with this period of no atmospheric holes which would be equivalent to a series of prelaunch laboratory images. This is a very important validation of the methodology for our identification of atmospheric holes. Comparison with Figure 2 for a period with substantial occurrence rates of atmospheric holes is instructive.

3.4. Effects of "Hot Spots" in the Pixel Array

For uniform illumination of the sensor of the Earth Camera the atmospheric holes should be randomly distributed among the pixels. Nonuniform sensitivities of groups of pixels can give rise to pixels which have an increased probability for satisfying the requirements for identification of an atmospheric hole. These pixels are referred to as hot spots in the pixel array. Images taken on the 4 days on June 1, 4, 7, and 10, 1997, are used to test for the hot spots. These 4 days are employed because the imaging at lower altitudes is acquired, along with the high-altitude viewing. Requirements for pointing the spacecraft platform often result in no viewing of dayglow from low spacecraft altitudes during an orbit.

Consideration of the results for a less restrictive set of search parameters relative to those adopted in the present work is instructive. These results are shown in Figure 4 for darkened pixels of clusters with five or more pixel members, a minimum decrease of −2 σ for each pixel and no restriction on the magnitude of the standard deviation. There are 65,536 pixels in the sensor array. The cumulative number of pixel locations is plotted as a function of the number of darkened clusters per pixel location. Thus, for example, there are four locations in the array which have 20 or more dark pixel clusters. Because the dayglow is not viewed evenly throughout the pixel map during an orbit but is favored for certain areas of the sensor, the expected random rate for no hot spots is computed by summing the corresponding Poisson distributions for a series of subsections of the sensor. These subsections cover the entire area of the sensor. Inspection of Figure 4 finds that there are approximately 600 hot spots, or about 1% of all of the pixel locations. Of course, the most important quantity is the percentage of darkened clusters associated with these hot spots, 27%, an unacceptably high percentage for a rigorous survey of atmospheric holes.

As discussed in a previous section the criteria for the detection of an atmospheric hole used in the present study is a cluster of 5 or more darkened pixels with intensity decreases ≤ −2.5 σ and a minimum standard deviation σ of 7.5 DN. The corresponding distribution of hot spots is shown in Figure 5 in the same format as previous Figure 4. For the present detection criteria, there are approximately 50 hot spots, or 0.08% of the entire pixel array. The corresponding percentage of darkened clusters associated with these hot spots is about 3%, an entirely acceptable value for our automated search.

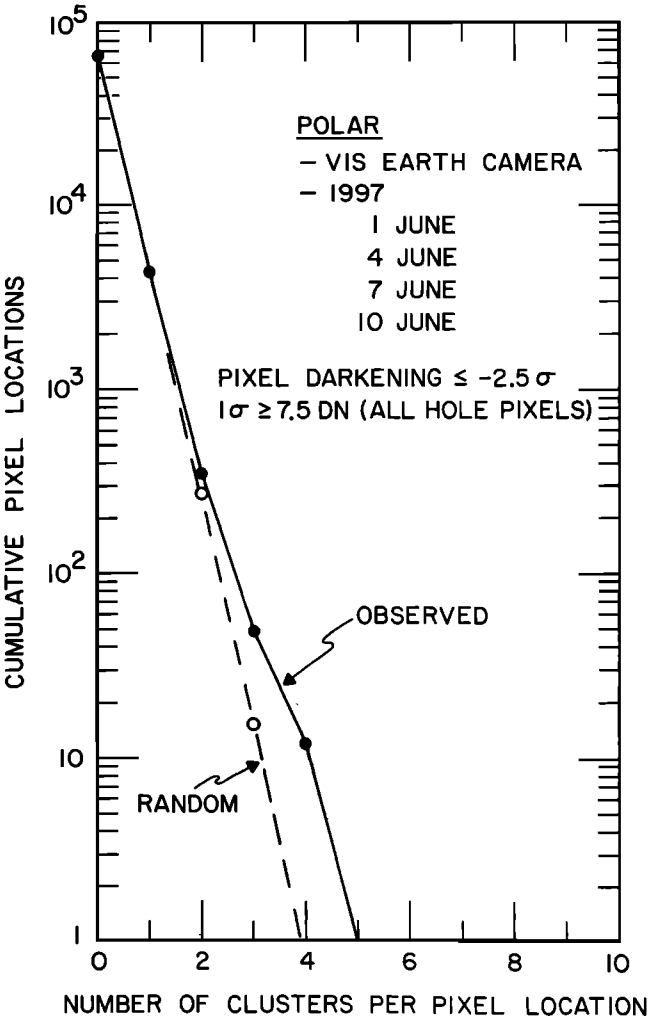

Figure 5. Continuation of Figure 4, but with pixel response decreases of ≤ −2.5 σ and a standard deviation ≥ 7.5 DN. These are the search criteria used for the automated detection of atmospheric holes in the present study. Note that the effects of hot spots are minimal, only about 3% of the entire set of darkened pixel clusters.

3.5. Effects of Charge Deposition Due to Penetrating Charged Particles in the Radiation Zone

During relatively short periods of the 17.6-hour orbital period of the Polar spacecraft the Earth Camera is viewing the dayglow while immersed in the energetic charged particle fluxes of the outer radiation zone. These periods range from about 10 to 25 min and are dependent on the spacecraft trajectory relative to the radiation zones. The corresponding altitude range of the spacecraft is about 2.5 to 3.5 R_E. In order to investigate

the possible effects of the charge deposition in the sensor of the Earth Camera due to penetrating electrons in the outer radiation zone the intensities of geomagnetically trapped electrons with energies of 2.7 MeV as simultaneously measured with the HIST instrument on the Polar spacecraft are employed (courtesy of J. B. Blake and R. S. Selesnick). This instrumentation is described by *Blake et al.* [1995]. The electron intensities exhibit large temporal variations and a major injection event associated with geomagnetic activity occurred on November 23, 1997. The range of electron intensities during the period October 30 to December 7, 1997, is sufficiently large to examine the threshold intensities for aliasing the automated detection of atmospheric holes.

The worst-case example of the effects of the penetrating electrons in the outer radiation zone is shown in the left-hand panel of Plate 2. This is a raw image with no corrections. It is obvious that about 30% of the pixel map is destroyed by the charge depositions in the pixels due to the energetic electrons which penetrate into the sensor of the Earth Camera. On the other hand, a raw image taken during a period of low electron intensities in the outer radiation zone is shown in the left-hand panel of Plate 3. Only one hole is found in this image. For such images the numbers of pixels affected by these electrons is minimal and will not significantly alias the automated search algorithm for identifying atmospheric holes.

It is important to discuss here the software algorithm which is used to mitigate the effects of the bright pixels which are associated with the penetrating charged particles. This algorithm is straightforward and easily implemented with a minimum aliasing of the pixel maps. The median for each pixel in an image is the median of the 49 pixels for the 7 × 7 pixel block which is centered on the pixel in question. If the response of this pixel is 30 DN or more above the median from the 49 pixels, then the pixel response is replaced by the median from the 49 pixels. The second step is the substitution of the corresponding medians for each of the 8 adjacent pixels to the bright pixel. That is, for each of these 8 pixels the 7 × 7 pixel block is centered on the pixel and the median is computed for the 49 pixels. There are other possible algorithms for removing the effects of the energetic particles, but this method has worked well for our automated hole search with a minimal number of false detections.

An atmospheric hole which was identified with the automated search is shown in each of Plates 2 and 3 for the worst and best cases, respectively. The images after the corrections for the penetrating particles are shown in the right-hand panels of the respective figures. Obviously for the best case in Plate 3 such corrections do not affect the character of the hole because of the sparcity of energetic electron events. On the other hand, for the worst case the density of these events in the pixel maps will affect the routine determinations of the means and standard deviations. In fact, detailed examination of the worst-case image reveals that the automated search with the corrections for the energetic particles identified 4 atmospheric holes correctly but generated 10 false holes. This situation is unsatisfactory and images corrupted with such high densities of energetic electron events are simply not usable.

In order to determine the threshold level of electron

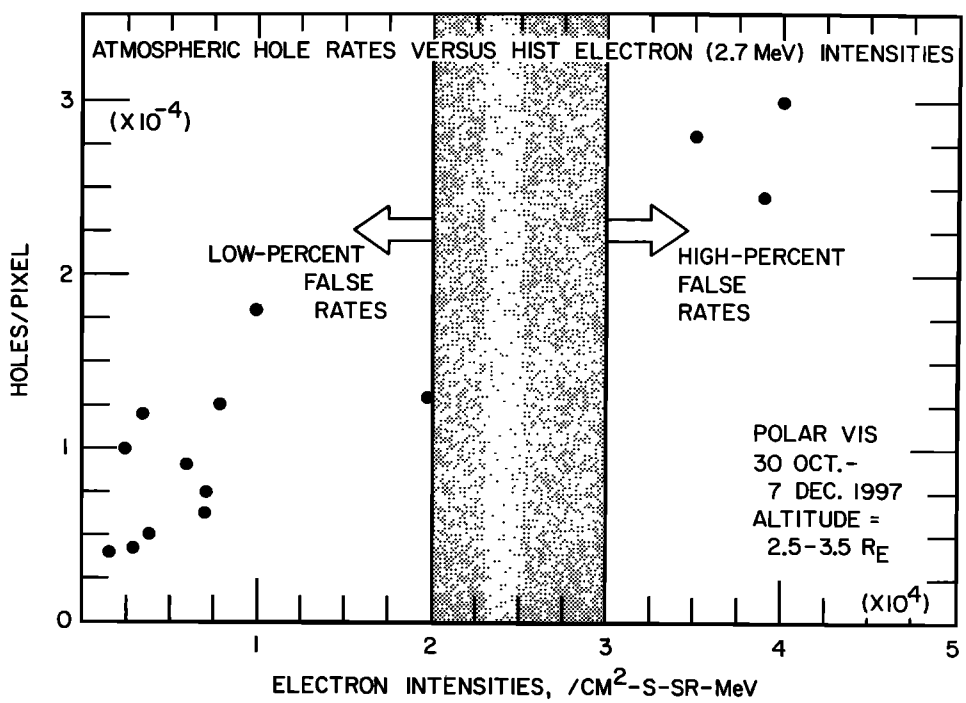

Figure 6. Atmospheric hole rates as observed with the Earth Camera on the Polar spacecraft plotted as functions of energetic electron (E = 2.7 MeV) intensities in the outer radiation zone (see text). The electron intensities were simultaneously measured with the HIST on board this same spacecraft (courtesy of J. B. Blake and R. S. Selesnick).

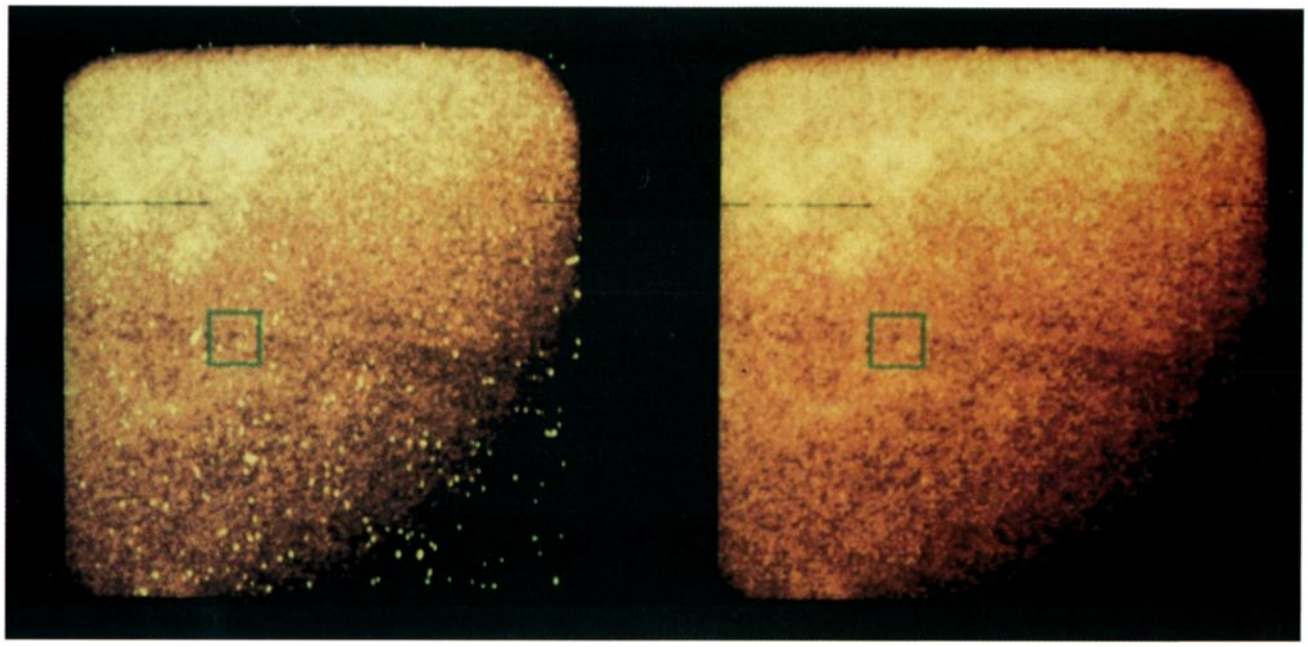

Plate 3. Continuation of Plate 2 for a period for which the energetic electron intensities in the outer zone were considerably lesser. An atmospheric hole is indicated by the boxes. Two thin horizontal lines are due to noise from the commutator between the camera platform and the spinning main body of the spacecraft. This image was taken at 0442:44 UT on November 22, 1997, at spacecraft altitude, latitude and longitude of 19,418 km, 30.2°N and 66.4°E, respectively.

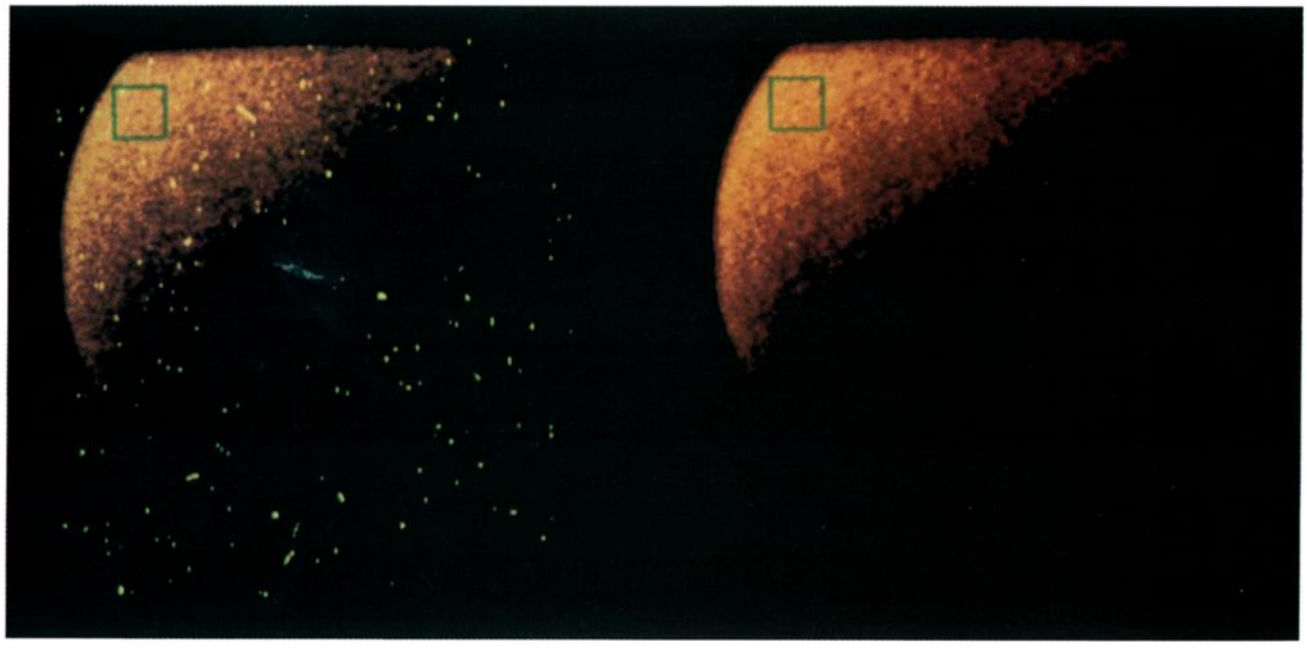

Plate 4. This image shows the typical radiation–induced effects outside of the radiation zones. The event rate is low and is due to penetrating cosmic rays. Thus most of the images are relatively free of the effects of intense charged particle radiation because the residence time in the radiation zones is 0.5 hours or less during the orbital period of 17.6 hours. This image was taken at 1954:06 UT on November 25, 1997, at spacecraft altitude, latitude and longitude of 32,706 km, 58.4°N and 191.1°E, respectively.

intensities in the outer zone which aliased the automated search into yielding a significant fraction of false identifications, the simultaneous measurements of the spin-averaged electron (2.7 MeV) intensities are used from the HIST. The frequency of atmospheric holes per pixel as observed with the Earth Camera are plotted as functions of the electron intensities in Figure 6. There is one data point per orbit. The statistical inaccuracies for these hole rates are $\leq \pm 30\%$. The maximum electron intensities for the traversal of the outer zone during the imaging sequence for the dayside atmosphere are used. For electron intensities $\lesssim 2 \times 10^4 (cm^2\ s\ sr\ MeV)^{-1}$ there is no correlation of pixel occurrence rates with the electron intensity. For example, for a hole rate of $\sim 1.2 \times 10^{-4}$ holes/pixel the electron intensities vary by a factor of ~10. On the other hand, the hole occurrence frequencies are abnormally high and approximately equal for electron intensities at $\sim 4 \times 10^4 (cm^{-2}\ s\ sr\ MeV)^{-1}$. This is the electron intensity level for the image in Plate 2. The search routines cannot be reliably used at these extremely high intensity levels. These periods with extremely high intensity levels are April 20–21, May 16–26, June 10–14, and November 23 to December 4, all during 1997. There were no HIST data during May 26 to June 5. The overall period studied in this report was April 1, 1997 through January 31, 1998. No data for the above periods of extremely high intensities are used in the present paper.

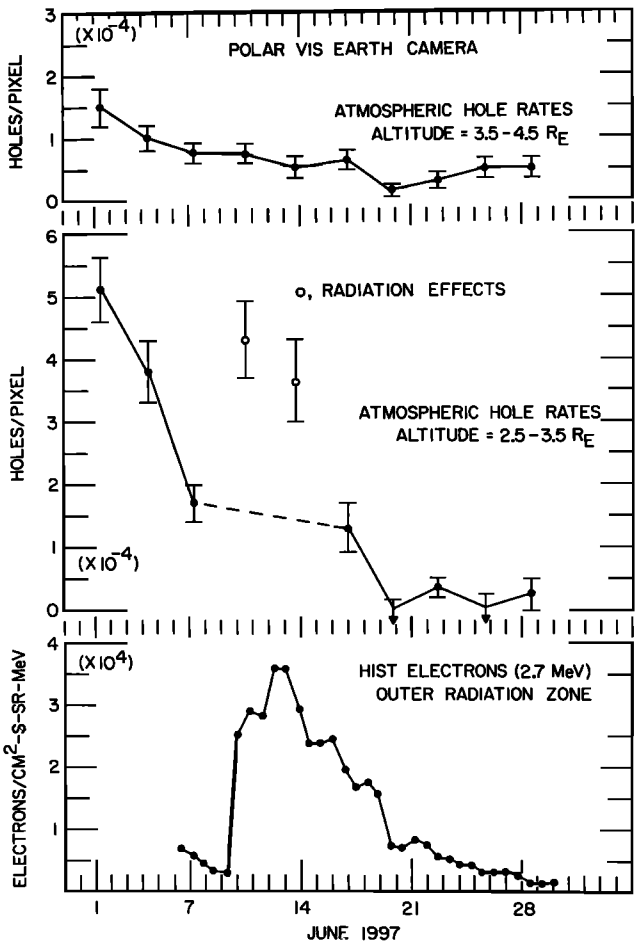

Figure 7. Comparison of the atmospheric hole rates (top) outside of the radiation zone, (middle) within the radiation zone, and (bottom) the maximum energetic electron rates in the radiation zone as measured with the HIST charged particle detectors. The automated search criteria prevent false identification of atmospheric holes unless the radiation intensities exceed high values in excess of $2 \times 10^4 (cm^2\ s\ sr\ MeV)^{-1}$.

Table 1. Pixels and Atmospheric Holes for the Radiation Belt Survey

Date,	Altitude, 2.5–3.5 R_E		Altitude, 3.5–4.5 R_E	
June 1997	Pixels ($\times 10^4$)	Holes	Pixels, ($\times 10^4$)	Holes
1	17.5	90	18.2	27
4	15.7	60	27.9	28
7	13.9	24	27.2	21
10	12.4	53	24.8	19
13	10.3	38	25.4	13
16	9.4	12	23.5	15
19	6.3	0	19.9	3
22	5.0	2	19.4	6
25	4.1	0	18.7	9
28	4.0	1	17.8	9

Further verification that the automated search criteria provides robust identifications of atmospheric holes in the presence of high intensities of energetic penetrating charged particles is given in Figure 7 for June 1997. In the upper and middle panels are shown the atmospheric hole rates for the specific area of the dayglow which was used for Figure 2 and later employed for the investigation of the altitude dependences of atmospheric holes in section 4.1. The spacecraft altitude range is 3.5 to 4.5 R_E for the upper panel and outside of the radiation zone, and the altitude range for the middle panel is 2.5 to 3.5 and deep within the radiation zones. The numbers of pixels and holes are given in Table 1. The higher hole rates in the lower altitude bin are due to an altitude effect (see section 4.1). The bottom panel shows the time profile for the maximum HIST electron intensities during the traversal of the radiation zone during which the Earth Camera images were being taken. A large electron injection event occurred on June 10, 1997, and provided an excellent opportunity to study the effects upon the images with respect to the determination of the atmospheric hole rates. The atmospheric hole rates inside and outside the radiation zone similarly declined with time with the exception of the period June 10–16 when the electron intensities exceeded $2 \times 10^4 (cm^{-2}\ s\ sr\ MeV)^{-1}$. Note that the atmospheric hole rate on June 7 was a factor of about 5 higher than on June 22 even though the radiation environment for the two days was the same. Thus the automated search criteria are remarkably effective in rejecting false events due to penetrating charged particles until a high-intensity level exceeding $2 \times 10^4 (cm^{-2}\ s\ sr\ MeV)^{-1}$ is reached.

Except for the relatively brief orbital segment during which the Polar spacecraft is in the radiation zone the cosmic ray fluxes are the main source of the contaminating charges in the sensor pixel array. These intensities

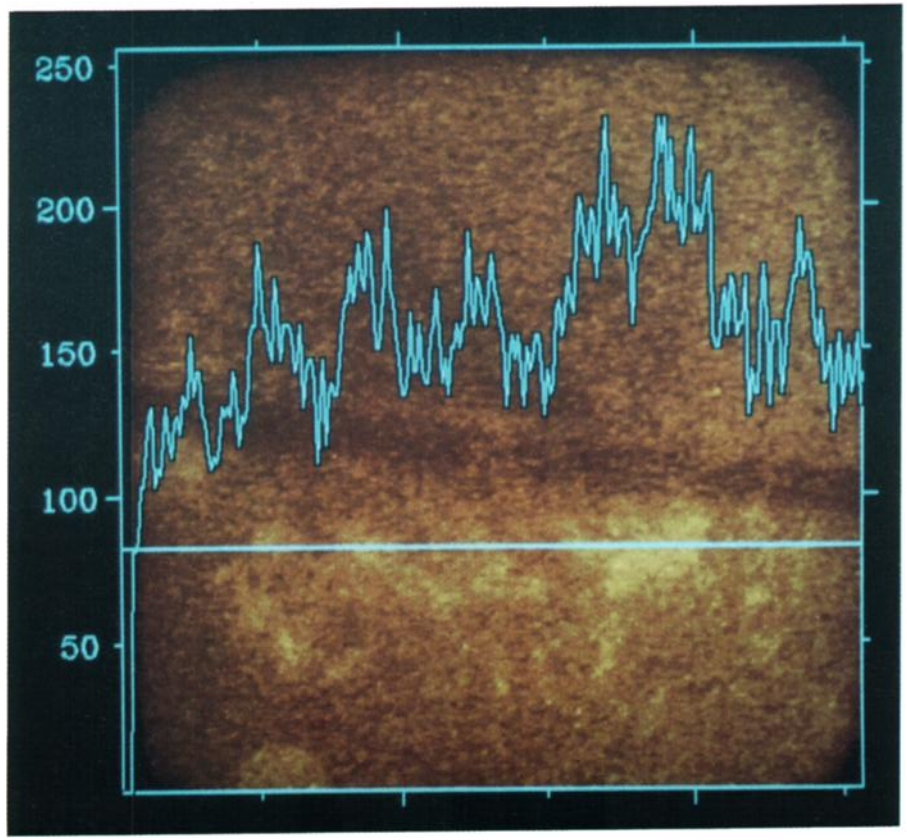

Plate 5. An image of the far–ultraviolet dayglow taken when the spacecraft was located at equatorial latitudes. Also seen in the image is a contribution in the near–ultraviolet due to the reflectance of sunlight from high–altitude clouds. A trace of pixel responses provides a quantitative assessment of the contributions from the clouds. The ordinate is in units of DN. This image was taken at 0213:19 UT on April 26, 1997, at spacecraft altitude, latitude and longitude of 11,448 km, −9.9°N and 134.6°E, respectively.

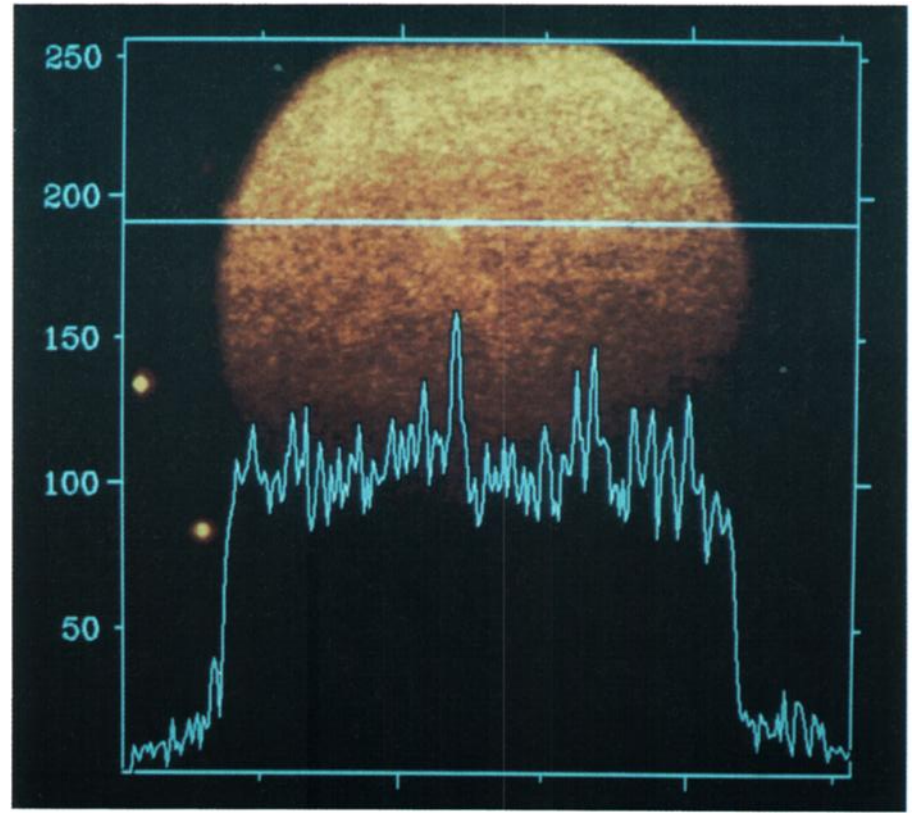

Plate 6. Continuation of Plate 5 for a spacecraft position at higher altitude and latitude. The trace of pixel responses crosses the limbs with no discernible increases. Thus the contributions of the optically thin emissions from O I 135.6 nm and the N_2 LBH bands are excluded by the passband of the filter. The trace also passes across a cloud. Typically less than 10% of the dayglow image exhibits the responses to high–altitude clouds. Two bright ultraviolet stars can be seen at the left in the image. This image was taken at 0614:58 UT on April 26, 1997, at spacecraft altitude, latitude and longitude of 41,947 km, 65.3°N and 82.5°E, respectively.

are relatively low and a typical example is shown in Plate 4 in the same format as the images in Plates 2 and 3, including the location of one of the two atmospheric holes. The effects of these charged particles are minimal and are typical of those seen over most of the orbit. These images without substantial contributions from penetrating energetic particles provide most of the basis for the studies of atmospheric holes reported here.

3.6. Long-Wavelength Contributions to the Responses of the Earth Camera

The spin-scan photometer on board the Dynamics Explorer 1 spacecraft which was used for far-ultraviolet observations of the dayglow and auroras employed a wide-band filter centered at a nominal wavelength of 130.4 nm for the investigations of atmospheric holes. This filter, specifically Filter no. 2, allowed the passage of several important emissions. A typical analysis showed that the responses were due to O I 130.4 (76.2%), O I 135.6 (8.6%), H I (13.0%) and N_2 LBH (2.0%) [*Craven et al.*, 1994]. Similar results were reported by *Gladstone* [1994] and *Meier et al.* [1995]. The above percentages could vary by 5% to 10% dependent upon the emission and the physical state and location in the upper atmosphere. For this filter, Rayleigh-scattered sunlight at wavelengths 180 to 300 nm was not an important contributor.

For the Earth Camera of the Polar spacecraft the passband was also nominally centered on the O I 130.4-nm emissions. This passband was narrower than that for Dynamics Explorer 1 and the contributions from O I 135.6, H I and N_2 LBH were significantly lesser and were not important contributors to the sensor responses for the investigations of atmospheric holes. However, the longer wavelength responses of the camera are important. An exemplary image of the dayglow which was taken when the spacecraft was positioned near the equator is shown in Plate 5. Bright features corresponding to the reflected light from the tops of high-altitude clouds are clearly seen in the image. Surface features such as continents and seas are not seen in the Earth Camera images which means that these longer wavelength responses are due to Rayleigh-scattered emissions in the wavelength range of about 200 to 300 nm.

The responses of the Earth Camera for a line trace through the image shown in Plate 5 provide a quantitative measure of the contributions of reflected light from the clouds. The ordinate is in units of DN. For the brightest cloud this contribution is about 40%. Thus the detection of atmospheric holes is compromised in part by these longer wavelength emissions. That is, the decrease in intensities in the holes due to absorption of the 130.4-nm emissions must be greater in order to overcome this increased background. On the other hand, these bright clouds typically cover about 5 to 10% of the sunlit Earth and hence the loss of the number of atmospheric holes is correspondingly small. We have used the 317-nm ozone filter of the Low-Resolution Visible Camera of the Polar spacecraft in order to provide a good upper limit on the longer wavelength radiation from off-cloud positions. The corresponding upper limit on the longer wavelength contribution is 15%. Hence most of the typical image seen in Plate 5 is usable for the detection of atmospheric holes due to the absorption of the 130.4-nm dayglow.

It is of further interest to similarly examine an image taken at higher altitudes. Such an image when the spacecraft was positioned at an altitude of 6.6 R_E is shown in Plate 6. Again, a pixel trace is given for a bright cloud feature. The cloud feature appears to be smaller than that shown in the above Plate 5 but that is primarily due to the fact that the spacecraft is at greater altitudes. As expected from the increased atmospheric path lengths for these images at higher latitudes, the brightnesses of the cloud tops are lesser, about 30%, and hence become of lesser importance as the spacecraft ascends to its polar apogee position. The reader should note that there is no limb brightening evident in the trace because optically thin emissions, such as O I 135.6 and N_2 LBH, are effectively excluded by the filter. Thus the Earth Camera provides a record of the O I 130.4 emissions, together with a contribution from high-altitude cloud tops. Because these bright cloud tops cover only a small fraction of the daylit atmosphere, the Earth Camera can be used for the detection of atmospheric holes in an automated mode.

It is also important to examine the positions of the atmospheric holes as determined with the automated search relative to the cloud features in order to ascertain that the atmospheric holes are not due to small-scale cloud features. Such examination of a series of images reveals that the atmospheric holes are more-or-less evenly distributed throughout the images. Thus the major fraction of the atmospheric holes cannot be attributed to cloud features because the cloud features cover a relatively small area of the image. It is found that only 5% or less of the atmospheric holes may be attributable to features at the edges of these high-altitude clouds and hence not due to 130.4-nm absorption.

3.7. Sigma Distributions

A plot of the frequency of pixel darkenings in an image as a function of the number M of standard deviations σ is expected to deviate significantly from random rates if there are atmospheric holes within the field of view of the camera. That is, no such deviation is clear evidence that the camera's responses are due to instrumental noise. Substantial deviations from the random rates can be due to a second instrumental effect or a geophysical phenomenon recorded by the camera. This issue is resolved by testing the events as to their correlations with spacecraft altitude, local time, meteor rates, etc.

For example, the frequency of occurrence of single dark pixels in the Dynamics Explorer 1 images as a function of the number M of standard deviations for their darkenings is shown in the top panel of Figure 8 [after *Frank et al.*, 1986a]. The bin size is 0.2 σ. About 1.3×10^6 samples of 130.4-nm dayglow are used for the measured occurrence frequencies. The mean rate for the pixel responses is 49 counts. A Poisson distribution with this mean and the corresponding $\sigma = 7$ counts is also shown in the upper panel of Figure 8. For $M > -3.0$ the pixel darkenings are accounted for as random events. The significant tail of the distribution for darkenings $M < -4.0$ is indicative of a second source of instrumental

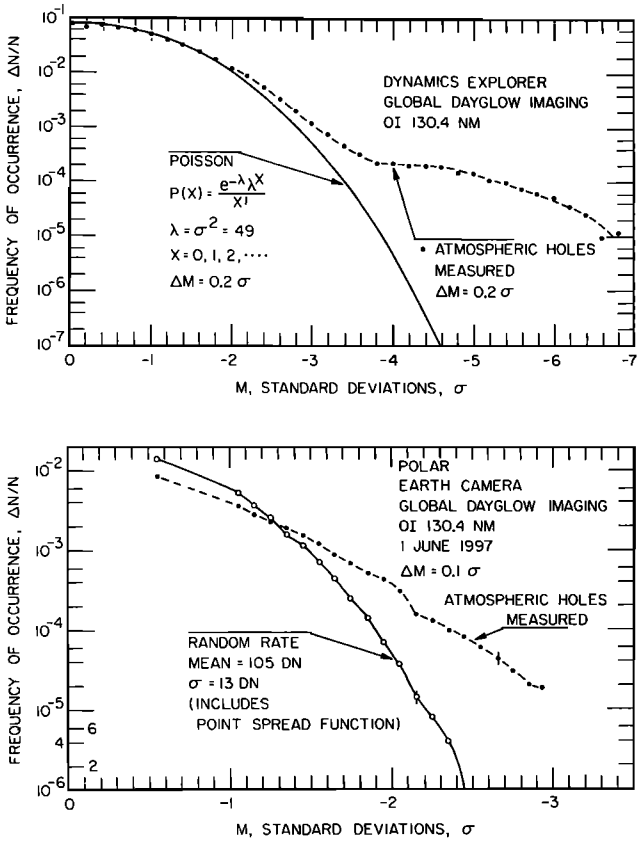

Figure 8. (top) The frequency of occurrence of single darkened pixels in the Dynamics Explorer 1 images as a function of the number of standard deviations for their darkening. Comparison with the Poisson distribution shows that the events with darkenings > −3.0 σ are dominated by statistical noise. The well-defined tail of the distribution at < −4.0 σ is associated with the presence of atmospheric holes [after *Frank et al.*, 1986a]. (bottom) The frequency of occurrence of five-pixel darkened clusters in the Polar Earth Camera images as a function of the number of standard deviations for their darkening. For darkenings of each of the five pixels > −1.6 σ the instrument responses are dominated by random events as shown with a comparison with the computed random rates based upon the known sensor characteristics. The well-defined tail of the distribution exhibits two components. The component with −1.6 σ to −2.0 σ is due mainly to artifacts such as sensor hot spots and penetrating radiation. The darkenings < −2.2 σ are due to the presence of atmospheric holes as shown by their strong geophysical corrclations which are presented in the paper.

noise or of real objects in the field of view of the camera. The geophysical correlations of these darkened pixels are used to eliminate the presence of a second source of instrument noise as summarized by *Frank and Sigwarth* [1993]. Thus atmospheric holes were established as real objects which appeared in the field of view of the camera.

Similar departures from a random distribution of clusters of darkened pixels are expected for the dayglow images taken with the Polar Earth Camera. This sensor is significantly different from the simple photon counter of the Dynamics Explorer 1 photometer. The random responses for the occurrence of 5-pixel darkened clusters for the Earth Camera must be calculated in three important steps. First, a Poisson distribution of photoelectrons is produced by the photocathode. Inflight calibrations find that the mean of this distribution is 157 electrons/pixel/image. Second, these photoelectrons are accelerated into the front face of chevron microchannel plates. The point spread function of these photoelectrons is closely approximated by a nine-pixel square array of fractional responses with 0.5 for the center pixel, 0.083 for the adjacent pixels, and 0.042 for the corner pixels. Third, is the inclusion of the spread of responses due to the electron multiplication within the microchannel plates, the phosphor responses and the CCD electronic noise, i.e., a Gaussian distribution with 1 σ = 9 DN. All of these constants used in computing the random rates are well determined.

The computed random rates for the occurrence of clusters of five darkened pixels as a function of the number of standard deviations for their darkening are shown in the bottom panel of Figure 8. Forty simulated images generated with the sensor characteristics as noted in the previous paragraph were used, each image an array of 256 × 256 pixels. The random rate at the CCD is characterized by a mean = 105 DN and a σ = 13 DN, and includes consideration of the point spread function. The statistical accuracy on the tail of the distribution is indicated by a vertical line. Within this statistical accuracy the curve is a smoothly declining function as a function of decreasing values of M. The criteria for the search remains the same as that for the corresponding search of the actual images. That is, each pixel response of the cluster must be ≤ −Mσ and σ ≥ 7.5 DN. For these calculations of occurrence frequencies careful consideration of the positions of the darkened clusters is necessary in order to avoid multiple counting of the same cluster.

As the values of M approach 0, the corresponding time to compute the frequency of occurrence rapidly increases. The calculation proceeds by differencing the integral occurrence frequencies for M and M − 0.1. That is, the bin widths are 0.1 σ. The random event rates as functions of numbers of darkened pixels in a cluster for a fixed value of M as shown in Figures 1, 2, and 3 are directly computed from the above set of simulated images.

The observed frequency of occurrence of clusters of five or more darkened pixels as a function of the decrease in intensities of Mσ or more is shown in the bottom panel of Figure 8 for the Earth Camera images taken on June 1, 1996. The width of the bins is 0.1 σ. For values of M > −1.6 the occurrence frequencies are similar to those calculated for the random rate. For M < −1.6, there are two tails in the distribution which significantly exceed the random rates. These two tails are to be found at about −2.0 < M < −1.6, and at M < −2.2. The appearance of these two tails is particularly gratifying because the analyses of instrument responses in the previous sections indicate that effects such as those due to energetic particles and sensor hotspots should contribute significantly to false detection of holes in the range −2.0 < M < −1.6 and indeed such a tail is present in the data shown in the bottom panel of Figure 8. The analyses of the preceding sections also show that these instrument

effects are not present for values of M < −2.5 which are positioned in the second tail of the distribution. Of course, in order to verify that this second tail is due to the presence of real objects within the field of view of the camera, and not due to another instrumental effect, it is necessary to establish the geophysical correlations associated with these darkened pixel clusters. These correlations are firmly established in the next sections. A factor of 2 for a threshold of M = −2.5 (Figure 8, bottom panel) is a good estimate of the accuracy with which the rates of large atmospheric holes can be determined. This accuracy due to choice of threshold is similar to that with the Dynamics Explorer 1 photometer (see Figure 1 of *Frank et al.* [1986a]).

4. Geophysical Effects

4.1. Altitude Dependence of Occurrence Rates of Atmospheric Holes

Several of the critics of the reality of atmospheric holes predict that the rates of atmospheric holes will be unaffected by the spacecraft altitude because they are instrument artifacts [*Parks et al.*, 1997; *Dessler*, 1991; *Cragin et al.*, 1987]. We refer in this paper to the Parks–Dessler–Cragin hypothesis that the atmospheric holes are instrument artifacts. That is, the number of holes per pixel will be constant regardless of the spacecraft position. For our present analysis the dayside of Earth is divided into 576 sectors of equal area at the upper atmosphere as is shown in Plate 7. The color-coded angular sectors are those which are viewed during the actual imaging series for June 1, 1997. The gray shading indicates regions of the dayglow which were not observed. The occurrence rates of atmospheric holes are indicated by the color scale on the right-hand side which is used to color the maps for two altitude ranges, 3 to 5 R_E and 5 to 8 R_E. A small amount of statistical fluctuations is introduced by using a random number generator in order to reflect the expected sampling statistics of an actual series of observations. The prediction of the artifact hypothesis is clear: there are no differences in the occurrence rates when the two altitude maps are compared. The unidentified instrument artifact must be blind to the spacecraft altitude.

The observations of the occurrence frequencies of atmospheric holes for June 1 are shown in Plate 8 in exactly the same format as Plate 7. The total number of atmospheric holes in the bins for 3 to 5 R_E and 5 to 8 R_E are 529 and 358, respectively. Recall that the orbital time at high altitudes near apogee is much greater than that for the lower altitudes. The altitude variations for the two maps are strikingly large. The occurrence rates are much less for the altitude bin at 5 to 8 R_E relative to those for 3 to 5 R_E. From the color bar note that the occurrence rates of atmospheric holes range from about 0.1 to 0.6 holes per 1000 pixels. The existence of a dramatic local-time variation favoring local morning sectors for both altitude bins is also evident in Plate 8. The instrument artifact hypothesis is inconsistent with the robust altitude and local-time effects observed in the maps for atmospheric hole rates.

It is worthwhile to further establish these results with the analysis of a second series of observations on June 4, 1997, four orbits after the observations of June 1. The reason for the fourth orbit selection is that the low-altitude observations are compromised during the intervening three orbits by the fact that the cameras are pointed in other directions than for dayglow measurements for the purposes of star viewing for calibration purposes or for viewing along the direction of the magnetic field, for examples. The occurrence rates for June 4, 1997, again in units of holes per pixel, are shown for the two altitude bins in Plate 9. The total number of atmospheric holes in the bins for 3 to 5 R_E and 5 to 8 R_E are 420 and 313, respectively. The presence of substantial altitude and local-time dependences similar to those for June 1 are confirmed with this second survey.

The altitude dependence of the atmospheric hole rates

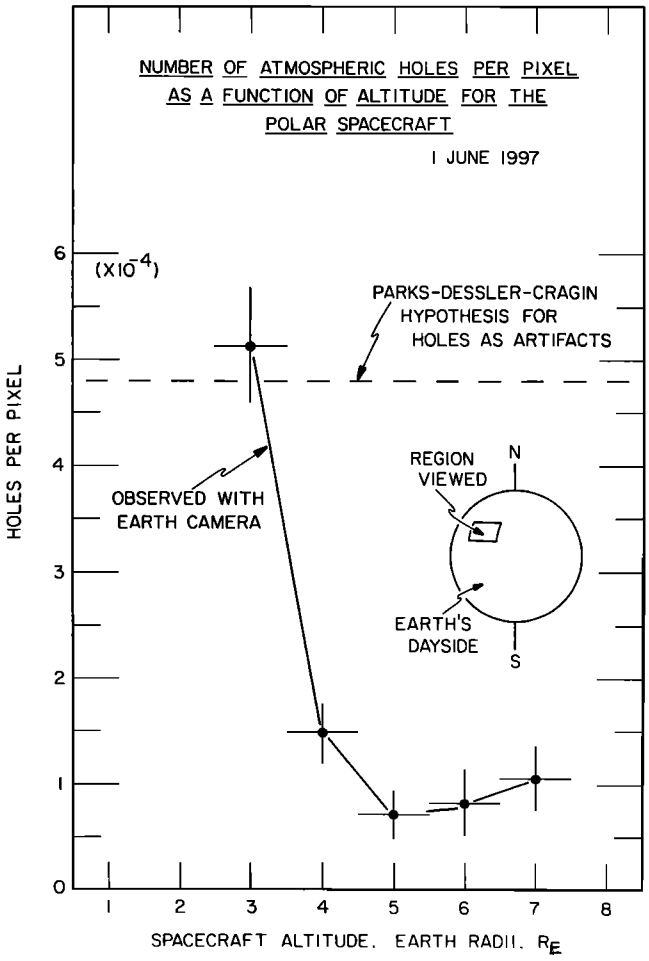

Figure 9. The observed dependence of the occurrence rate of holes per pixel as a function of altitude in 1–R_E bins on June 1, 1997. The 12 angular sectors in the atmosphere which were used are shown in the right-hand side of this figure. The Parks–Dessler–Cragin hypothesis for holes as instrument artifacts requires that there is no dependence on altitude and is shown as a horizontal line at an arbitrary value. The measured altitude dependence is large and eliminates the possibility of instrument artifacts. The slight increase in the 6–R_E and 7–R_E bins is further evidence that the holes are real objects because this effect is expected for the large slant angles for viewing the selected atmospheric region.

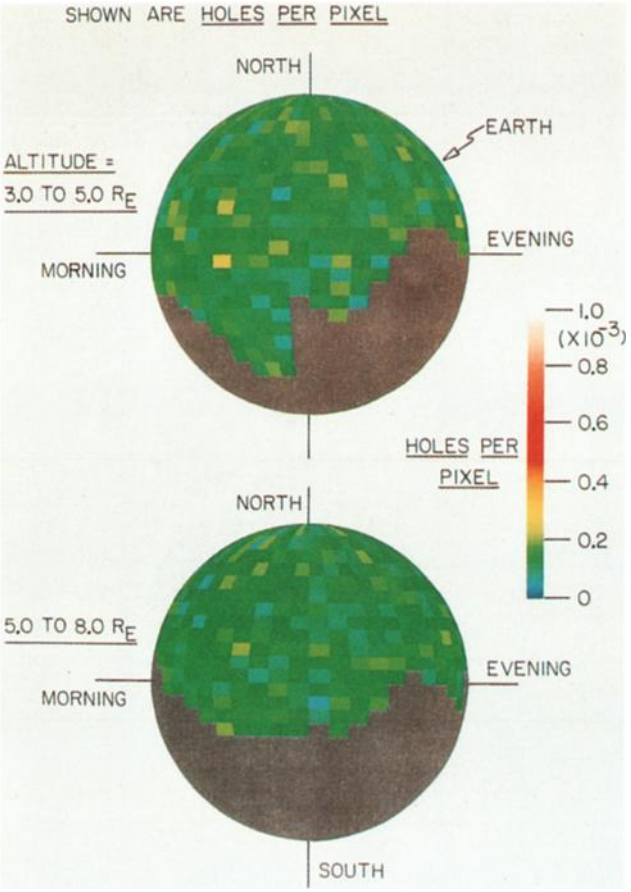

Plate 7. Expectations from the Parks–Dessler–Cragin hypothesis that states that the atmospheric holes in the images from the Earth Camera are instrumental artifacts. According to this hypothesis there can be no variations in the occurrence rate of atmospheric holes per pixel as a function of spacecraft altitude or the local time of the dayglow emissions. Thus the maps of hole frequency for the two altitude ranges, 3.0 to 5.0 R_E and 5.0 to 8.0 R_E, should be identical with the exception of small fluctuations due to hole counting statistics. The area of the sunlit atmosphere is divided into 576 sectors with equal areas. The sectors which are sampled with the Earth Camera on June 1, 1997, are identified by the color bar on the right-hand side and the sectors which were not viewed are indicated by the gray color.

is further examined for June 1 and 4, 1997, in Figures 9 and 10, respectively. The occurrence rates are plotted for five 1–R_E bins for the 12-sector area of the atmosphere as noted in the two figures. If the subsolar coordinates are (0°, 0°) then the corner coordinates (latitude, longitude) for the viewed area are (14.5°, −52.5°), (30.0°, −52.5°), (30.0°, −22.5°), (14.5°, −22.5°). It is very important to note that a specific atmospheric area must be selected because of the strong local-time dependences of the rates as is evidenced in the maps of Plates 8 and 9. Otherwise, a study of the altitude dependence simply on the basis of spacecraft altitude is compromised by the local-time variations and the changing viewing geometry along the spacecraft orbit. The changing viewing geometry along the orbit is dramatically demonstrated by comparison of the images in Plates 2, 3, and 4. The error bars shown in Figures 9 and 10 correspond to ±1 σ. The Parks–Dessler–Cragin hypothesis is shown in Figure 9 only. It predicts that the occurrence rates must be constant as a function of altitude. Of course, the absolute rate is not predicted and is arbitrarily assigned in our graphs. The strong observed variations of rates as a functions of altitude reject the instrument artifact hypothesis.

It is interesting to note that there is a minimum in the occurrence rates at an altitude of about 5 to 6 R_E for both of the measurement sets on June 1 and 4, and that the rates increase slightly for the higher altitude bins centered at 7 R_E. If the atmospheric holes are a real geophysical phenomenon, this increase must occur because of the large slant angles from the spacecraft to the targeted region. These slant angles, angles between the normal to the region viewed and the line of sight, are given in Table 2. This table also gives other orbital and viewing parameters for the images closest to the centers of the 1–R_E bins.

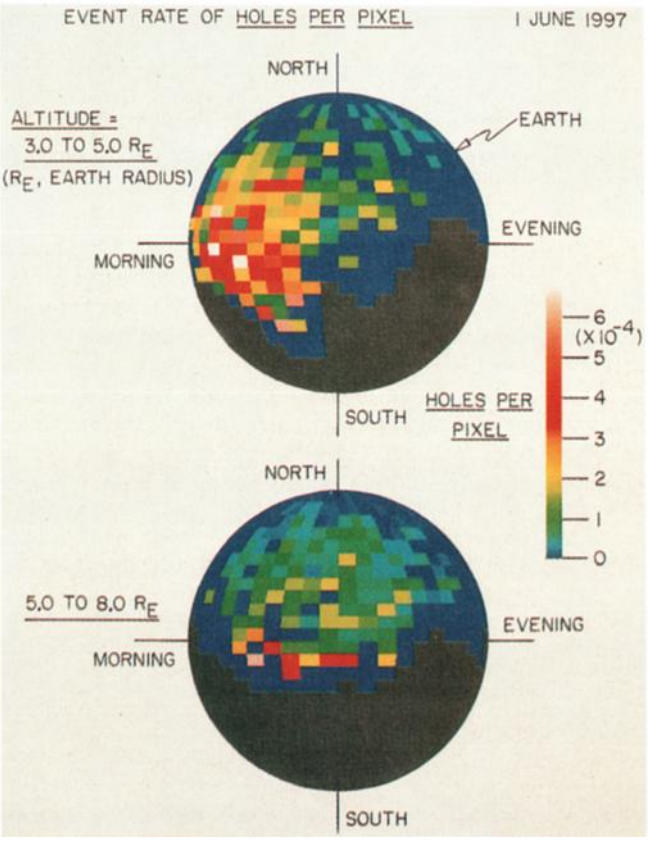

Plate 8. In the same format as shown in Plate 7 the observations of atmospheric holes with the Earth Camera on June 1, 1997, are displayed. The distributions of the occurrence rates of holes per pixel exhibit a strong altitude dependence and a local-time variation which favors the local-morning sectors of the dayside atmosphere. The instrument artifact hypothesis as shown in Plate 7 fails to account for these altitude and local-time dependences. The atmospheric holes must be due to geophysical effects, and not due to instrument artifacts.

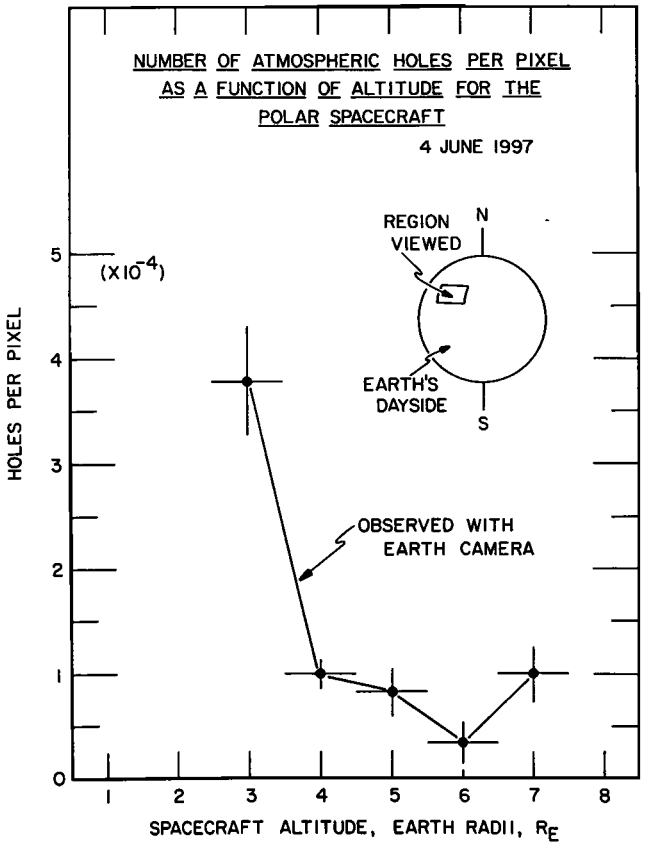

Figure 10. Continuation of Figure 9 for June 4, 1997.

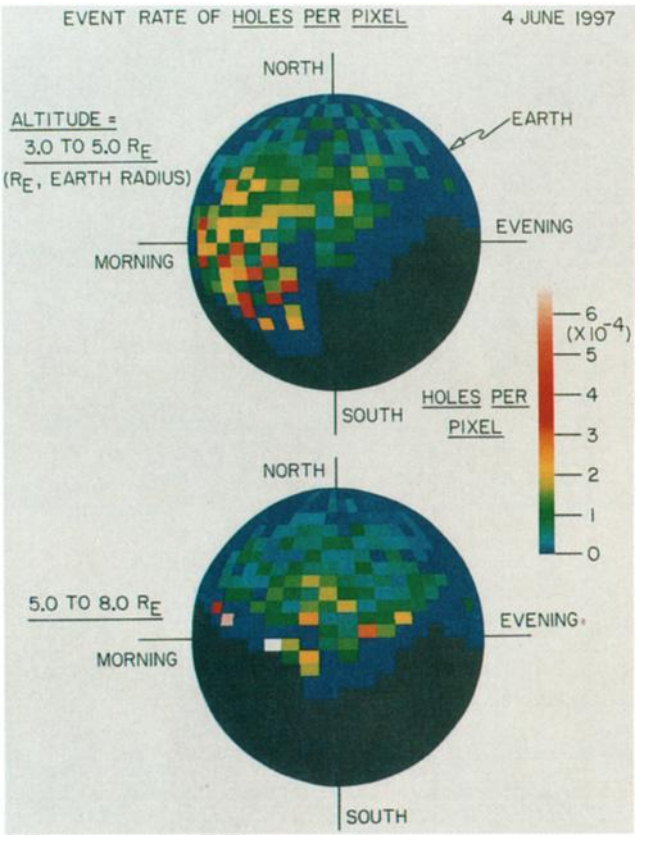

Plate 9. A continuation of Plate 8 for the occurrence rates of holes per pixel but for the later date of June 4, 1997. With the exception of the changes in occurrence rates associated with seasonal variations, the maps are similar to those for June 1.

Note that the ratios of the occurrence rates for 3 and 5 R_E, for examples, are similar for the two series of measurements on June 1 and 4. All available images are used for June 1 and 4; there is no editing of the images. In fact the atmospheric hole rates have decreased by about 25% on June 4 relative to those on June 1. As noted in the previous section careful consideration of the radiation belt intensities in the bin at 3 R_E is necessary in order to eliminate aliasing of hole observations at high electron intensities. The HIST electron (2.7 MeV) measurement on June 7, 1997, was ~5 × 10^3 cm^2 s sr MeV and well below the threshold for such aliasing. However, HIST energetic electron measurements were not available for June 1 and 4. Thus the electron (2.5 – 14 MeV) meas-

Table 2. Viewing Angles and Dayglow Intensities for Several Spacecraft Altitudes

Spacecraft Altitude, R_E	Spacecraft Latitude, °N	Spacecraft Longitude, °E	Spacecraft Local Time, LT	Solar Zenith Angle, deg	Sun–Atmosphere–Spacecraft Angle, deg	Angle Between Atmospheric Normal and Direction to Spacecraft, deg	Dayglow Intensity, kR
			June 1, 1997				
3	19	142	0854 LT	43	45	20	17.2
4	34	39	0902 LT	43	40	3	14.1
5	46	28	0907 LT	43	43	16	14.2
6	58	13	0915 LT	43	48	29	14.2
7	69	356	0928 LT	43	54	40	14.4
			June 4, 1997				
3	19	160	0842 LT	43	48	21	15.8
4	35	54	0850 LT	43	43	1	14.2
5	46	43	0855 LT	43	43	15	13.9
6	57	30	0902 LT	43	49	27	13.2
7	68	12	0916 LT	43	55	38	13.7

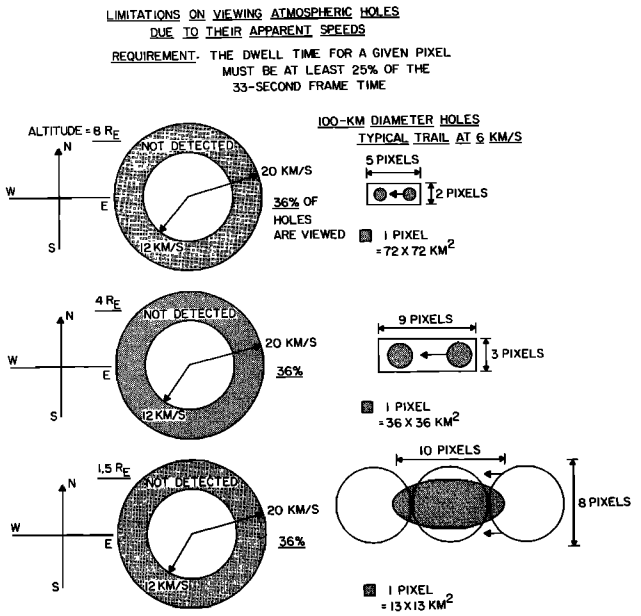

Figure 11. The average number of holes per sector for each Earth Camera image as a function of spacecraft altitude on June 1, 1997.

urements with the PET instrumentation [*Cook et al.*, 1993] on board the SAMPEX spacecraft were used to confirm that the electron intensities during June 1 and 4 were similar to those for June 7, i.e., there was no major electron injection event. Because the operating parameters for the Earth Camera were identical for these two days these temporal variations of hole rates are further evidence against an instrument artifact as a source of atmospheric holes (see also Figure 7). That is, the camera would be unaware of the date.

Because the atmospheric holes have been shown here to be a geophysical phenomenon and are not due to an instrument artifact, it is more appropriate to replot the results shown in Plates 8 and 9 in terms of events per sector as averaged over the number of images of that sector. Such a plot compensates for the decreasing projected areas of the sectors with increasing slant angle for the measurements. Such a map for June 1 is shown in Plate 10. For example, the upper map provides an approximate measure of the number of holes which would be detected in the 33-s accumulation period of an image as averaged over the altitude range of 3 to 5 R_E. For a hole lifetime of about 100 s [*Frank and Sigwarth*, 1993, 1997a] these maps provide an approximate record of the number of atmospheric holes occurring per minute, within factors of 2 to 3. The map for June 4 is shown in Plate 11. The high-altitude maps record only a small fraction of the actual events because the apparent sizes of the atmospheric holes as viewed from these altitudes are similar to the pixel resolution of the Earth Camera. Thus an approximate value of the global event rate from the low-altitude map of Plate 10 is in the range of tens per minute, in agreement with ranges for global event rates as previously determined with the spin-scan imager on board Dynamics Explorer 1 [*Frank and Sigwarth*, 1993].

Similar conversion of Figures 9 and 10 to units of atmospheric hole events per angular sector as averaged over the number of times that the area was viewed is shown in Figures 11 and 12. The same area of 12 angular sectors is used in order to acquire adequate event counting statistics and to avoid aliasing the results due to the substantial local-time dependences. The expected decreasing rate is evident in Figures 11 and 12 because the slant range effects to be seen in the high-altitude bins in Figures 9 and 10 are reduced by assigning equal areas of the atmosphere for each angular segment.

4.2. Local-Time Variations of Occurrence Rates of Atmospheric Holes

The diurnal (local-time) variations of the number of holes per angular sector as averaged over the number of images of that sector are shown in Figure 13 for a solar-ecliptic latitude band at 14.5°N to 30°N on June 1, 1997. This local-time effect is readily noted in Plate 10. The local-time dependence for the two altitude bins, 3 to 5 R_E and 5 to 8 R_E, favors the late-morning hours as shown in Figure 13. The occurrence rates for the high-altitude bin have been multiplied by a factor of 5 in order to accommodate the decrease of rates with altitude. It is important to consider that the spacecraft viewing geometries for the two altitudes are significantly different. For the low-altitude bin the spacecraft trajectory passes over the dayglow during the morning hours and for the high-altitude bin the dayglow is viewed from high latitudes and altitudes. Both of these views find a maximum of hole occurrence rates at local morning, about 1000 LT, relative to those at local evening.

It is important to ascertain that the local time effect for

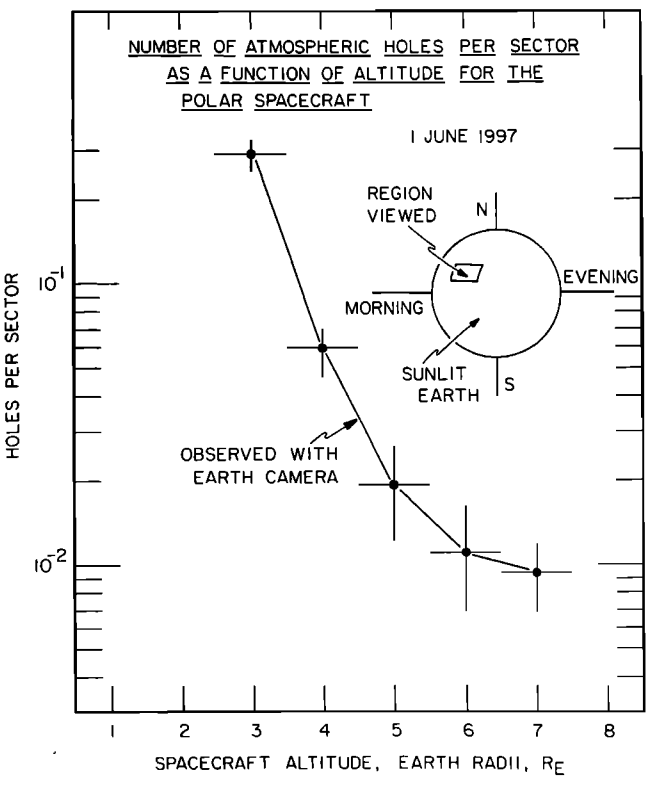

Figure 12. Continuation of Figure 11 for June 4, 1997.

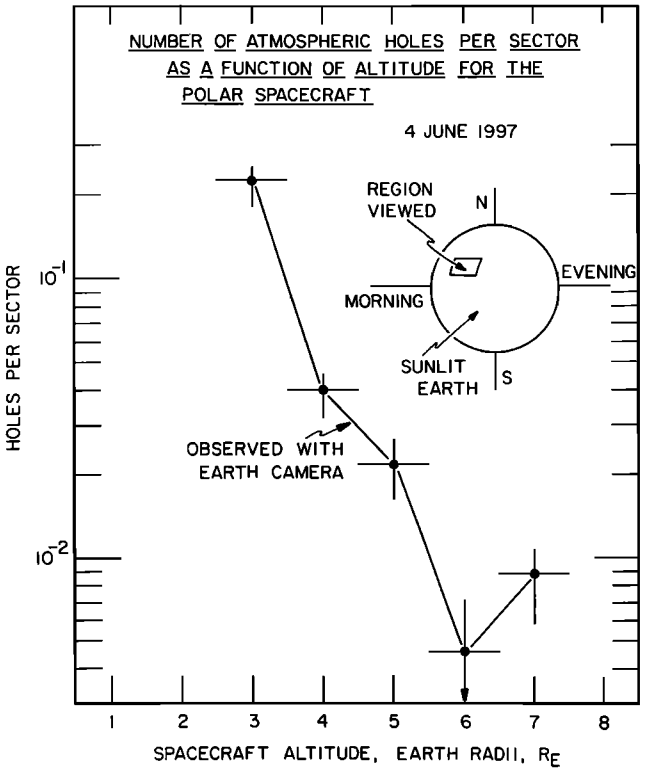

Figure 13. The diurnal variations of the number of atmospheric holes per sector for the latitudinal zone of 14.5°N to 30°N in solar ecliptic latitude. The diurnal variations are given for the two altitude bins shown in Plate 10. Note that the diurnal variations favoring local morning are also seen in the highest altitude bin, even though the occurrence rates are much less.

the low-altitude bin in Figure 13 is not dominated by the fact that the spacecraft trajectory passes over the morning sector of the dayglow, i.e., a nadir effect. The possibility of the dominance of a nadir effect can be investigated by examining the local-time dependence in the narrower altitude bin of 3.5 to 4.5 R_E which is fortuitously positioned such that the spacecraft nadir direction nearly coincides with atmospheric normal (see Table 2). The observed diurnal variations in this altitude bin for the solar ecliptic latitude band 9.6°N to 35.7°N, which is increased to improve counting statistics, is shown in Figure 14. If the hole rates were due primarily to the nadir effect, the maximum rates should coincide with the local time of the spacecraft. However, the local time of the spacecraft position does not coincide with the maximum of the hole rates. Thus substantial local-time variations in these hole rates are observed at these altitudes.

A similar local-time dependence of atmospheric hole rates was observed with Dynamics Explorer 1 in a different orbit and with a camera of entirely different design. Again, these local-time variations cannot be accounted for by instrumental artifacts.

4.3. Increasing Apparent Sizes of Atmospheric Holes With Decreasing Spacecraft Altitude

The major features of atmospheric holes have been already established in the published literature [*Frank and Sigwarth*, 1993, 1997a]. Of interest for the present discussion are the facts that (1) the atmospheric holes expand to maximum diameters of about 100 km, (2) the expansion rate of the diameters is about 1 km/s, (3) the lifetime of the atmospheric holes is about 100 s, and (4) the apparent speeds are in the range of 0 to 20 km/s.

Without the need for invoking a detailed model for the atmospheric hole the above features can be used to provide the expectations for viewing atmospheric holes with the Earth Camera as a function of spacecraft altitude. These expectations are shown in the diagrams of Figure 15. First of all the reader should note that the dwell time of an atmospheric hole on a given pixel of the camera must be at least about 25% of the image accumulation time of 33-s because the 2.5-σ decrease for the threshold of a darkened pixel corresponds to approximately a 25% decrease in the pixel responses. Shorter dwell times on a pixel produce darkenings which are less than this threshold and cannot be robustly detected in the images. Hence, for a given altitude there is a maximum apparent speed (trail length) for which a hole can be detected with the Earth Camera. Because the apparent sizes and speeds in terms of pixels increase with decreasing altitude, the maximum apparent speed is more or less a constant as a function of spacecraft altitude. This speed is 12 (± 3) km/s. Thus the corresponding percentage of the atmospheric holes which can be detected is 36 (+13, −11)%. For simplicity, it is assumed that the apparent velocities are distributed uniformly in direction where in

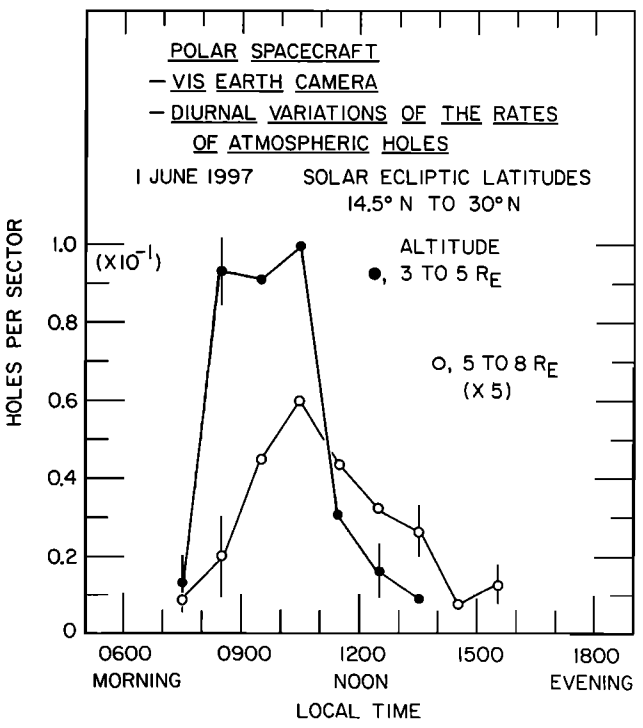

Figure 14. Atmospheric hole rates as a function of local time for the altitude bin 3.5–4.5 R_E and the solar ecliptic latitude band 9.6°N to 35.7°N on June 1, 1997. If the hole rates were dominated by the nadir effect, rather than that due to local time, the spacecraft position would be symmetrically placed at the maximum in the hole rate profile.

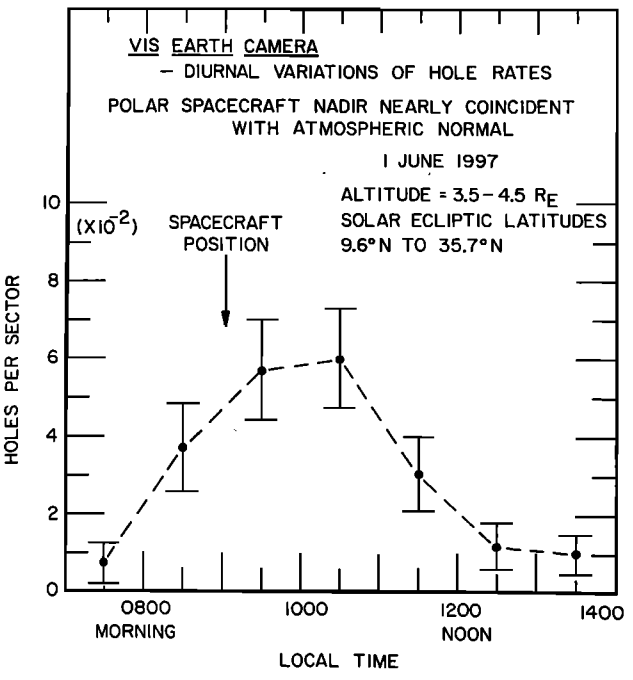

Figure 15. Diagram which shows the expected increases in the maximum sizes of atmospheric holes in the images as the spacecraft altitude decreases. Exemplary pixel dimensions are given for an atmospheric hole diameter of 100 km and an apparent speed of 6 km/s.

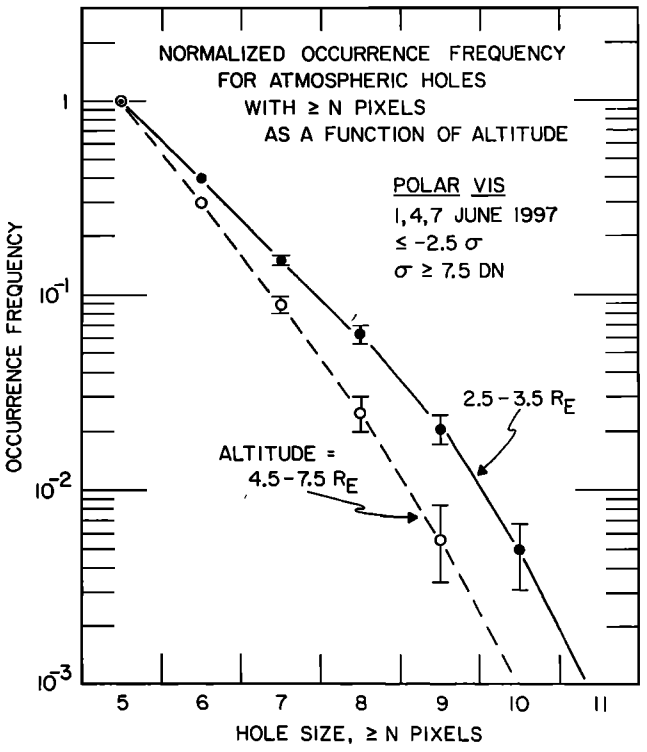

Figure 16. Normalized occurrence frequencies as a function of hole size as measured in numbers of pixels as observed during June 1, 4, and 7, 1997. The apparent hole sizes are larger for the lower altitude bin at 2.5–3.5 R_E relative to those observed in the 4.5–7.5 R_E bin as expected for atmospheric holes located in the upper atmosphere.

fact there is a preferred direction of motion from east to west across the daylit hemisphere of Earth [*Frank and Sigwarth*, 1993, 1997a].

Second, the expectations for the sizes of the darkened pixel clusters can be understood by the diagrams on the right-hand side of Figure 15 for the three spacecraft altitudes of 8, 4, and 1.5 R_E, respectively. A diameter for the atmospheric hole of 100 km is assumed, along with an assumed apparent speed of 6 km/s as an example. The pixel dimensions are also given in the figure. Because the full width of the point spread function at one-half maximum response is about 2 pixels as determined by viewing stars [*Frank and Sigwarth*, 1997c] the trail of the atmospheric hole will be smeared into a thickness of about two pixels and many of the holes will not be detected when viewed from the highest altitudes. The motion of an atmospheric hole during the 33-s sampling period is shown for all three altitudes, as well as the apparent size of the hole. The pixel dimensions are given in the same scale in order to facilitate the comparison for the different altitudes. At lower altitudes of 4 R_E the atmospheric hole is resolved as shown in the pixel diagram on the right-hand side of Figure 15. The low-altitude case for viewing an atmospheric hole from a range of 1.5 R_E is also interesting. The hole is large and the requirement for a pixel darkening of 25% yields an elliptical feature in the pixel map with a membership of about 50 pixels. Three circles are drawn for the atmospheric hole in this diagram and correspond to the position of the atmospheric hole at the beginning and end of the image frame and a center circle for the position of the atmospheric hole at midframe. It turns out that the apparent motion of 6 km/s during the frame accumulation of 33 s corresponds to an apparent motion of 198 km, or two hole diameters, which explains the relative hole positions shown in Figure 15. Later in this section such large features are reported.

Table 3. Occurrence Frequencies of Atmospheric Holes Per Pixel for 1-R_E Altitude Bins on April 26, 1997

Spacecraft Altitude, R_E	Holes/Pixel, $\times 10^{-5}$
1	2.8 (± 0.4)
2	7.4 (± 0.5)
3	13.8 (± 2.0)
4	3.3 (± 0.4)
5	2.4 (±0.3)
6	2.1 (±0.3)
7	1.7 (±0.3)

In summary, as the spacecraft altitude decreases from apogee position at 8 R_E, the frequency of detection of the atmospheric holes will increase because the apparent sizes of the holes are larger. Thus the occurrence rates recorded with the Earth Camera should increase, then decrease with decreasing spacecraft altitude if the holes are a geophysical effect. Indeed, this effect is clearly seen in the altitude dependence of the hole occurrence

rates shown in Table 3 for April 26, 1997, for seven 1-R_E altitude bins positioned at 1 to 7 R_E. The radiation environment for this series of measurements was not severe and is only present during the bin at altitude 3 R_E. Note that the increases and decreases in the adjacent altitude bins also exhibit the expected behavior and are positioned outside of the radiation zone. All pixels with dayglow are used for this survey because there is no single daylit sector which is viewed for all of these altitudes. In fact, the viewing encompasses both the Northern and Southern Hemispheres. The effect is sufficiently robust as to overcome the latitude and local-time dependences of the atmospheric hole distributions. Note that the instrument artifact hypothesis demands that the hole rates shown in Table 3 do not change with altitude.

The rapid decrease in the atmospheric hole rates at the lower altitudes is precisely what is expected for a real geophysical phenomenon and cannot be explained in terms of an instrument artifact. This decrease is due to the fact that the atmospheric area in an image, in km^2, is rapidly decreasing with decreasing altitude with a corresponding decrease in the numbers of holes present in each image.

The increases of the sizes of atmospheric holes can be directly determined for viewing the same dayglow area by comparing the occurrence frequencies of hole sizes for two altitude bins, 2.5 - 3.5 R_E and 4.5 - 7.5 R_E, as shown in Figure 16. This dayglow area is the same as that employed for the altitude study (see Figure 9). The occurrence frequency is normalized to that for 5-pixel holes because the direct comparison of the larger hole sizes is of importance. Three days of data gathering, June 1, 4, and 7, 1997, are used in order to improve the statistical significance of the altitude dependence of the hole sizes. Note that the occurrence of holes with nine or more pixels is a factor of 4 greater in the lower altitude bin relative to the bin at higher altitudes with a statistical significance of about 10 σ.

Of course, an exciting aspect for this investigation of hole sizes is the promise of the observations at the lowest altitudes as displayed in the bottom panel of Figure 15 which shows that atmospheric holes with pixel membership in the range of 40 to 50 darkened pixels should be occasionally sighted at altitudes of $\lesssim$ 1.5 R_E. Accordingly, a set of 50 images taken at low altitudes and selected only on the basis of good dayglow viewing geometry was examined for the presence of large atmospheric holes. The images were taken during April 23 and 26, and May 1, 1997. The spacecraft is moving quickly through these southern locations near its perigee and imaging time is limited. Still, it was gratifying to find 5 large atmospheric holes in these 50 images.

A raw image, with the exception of the removal of energetic particle events in the sensor, is shown in Plate 12. None of these charge depositions from energetic particles compromised the atmospheric hole indicated with an arrow and there were no clouds in its vicinity. Even though the atmospheric hole comprises about 50 darkened pixels it appears relatively small in the image simply because of the 65,536 dayglow pixels in the image. The pixel resolution is 11 km, and the dimensions of the atmospheric hole are about 100 km, as expected. A pixel map of the event with responses in standard deviations is shown in Plate 13. The color code is linear as a function of standard deviations and is such that yellow is > 0 σ and brown is -3.0 σ. This event is so large that it aliases the determination of the standard deviations and means which have been computed for a box which has been increased from 7 × 7 pixels in our standard computation to a box of 13 × 13 pixels. For a threshold of 0 σ one would expect equal numbers of yellow and darkened pixels surrounding the hole. The predominantly yellow pixels in the surrounding region are due to the fact that the mean is underestimated and that the pixels are somewhat darker than computed with even a search box of 13 × 13 pixels. In any case, the size of the hole is about 50 pixels. A second example of a slightly smaller atmospheric hole in numbers of pixels is shown in Plate 14 where yellow indicates $\leq$ -0.5 σ and brown is -3.0 σ. The pixel dimension is 18 km. The diameters of the clusters of darkened pixels are about 100 km, as expected.

4.4. Seasonal Variations of Atmospheric Hole Rates

It is of considerable interest to compare the seasonal variations of the occurrence rates of atmospheric holes as observed with the far-ultraviolet photometer on board Dynamics Explorer 1 with those as determined with the Earth Camera of the Polar spacecraft. The Dynamics Explorer 1 observations of seasonal variations for the period November 1, 1981, through late-January 1982 are shown in the top panel of Figure 17 [*Frank et al.*, 1987; *Frank and Sigwarth*, 1993]. The area for the events is bounded by solar-ecliptic latitudes and longitudes 30° to 90° and 285° to 315°, respectively, for a total area of 1.1 × 10^7 km^2. The occurrence rates averaged over 2-day periods are shown in Figure 17. The overall variations are large, i.e., by a factor of 10. The principal features of the atmospheric hole rates are a maximum intensity during early November, a brief plateau of intensities in mid-November, more or less constant intensities during November 21 until December 14, a lower plateau of intensities during December 14 through early January, and a well-defined minimum in mid-January with subsequent recovery. Certainly, these are enough features to establish a correlation with other observations, if one exists.

In the bottom panel of Figure 17 are shown the forward scatter radar rates for the same months at Ottawa, Canada [*Vogan and Campbell*, 1957], but for a period 26 years earlier than the Dynamics Explorer 1 observations. It is quite evident that the atmospheric holes are not correlated with the well-known stony meteor showers but are instead well correlated with the nonshower rates indicated by the solid circles. Forward scatter radar signals are more sensitive to higher altitude events relative to the infall of the meteors associated with the showers [*McKinley*, 1961]. The maximum nonshower rates during early November, the two main plateaus of rates during mid-November through early January, and the minimum in mid-January with subsequent recovery are well correlated with the Dynamics Explorer 1 detections of atmospheric holes in the upper panel of Figure 17.

The atmospheric hole rates as observed over the

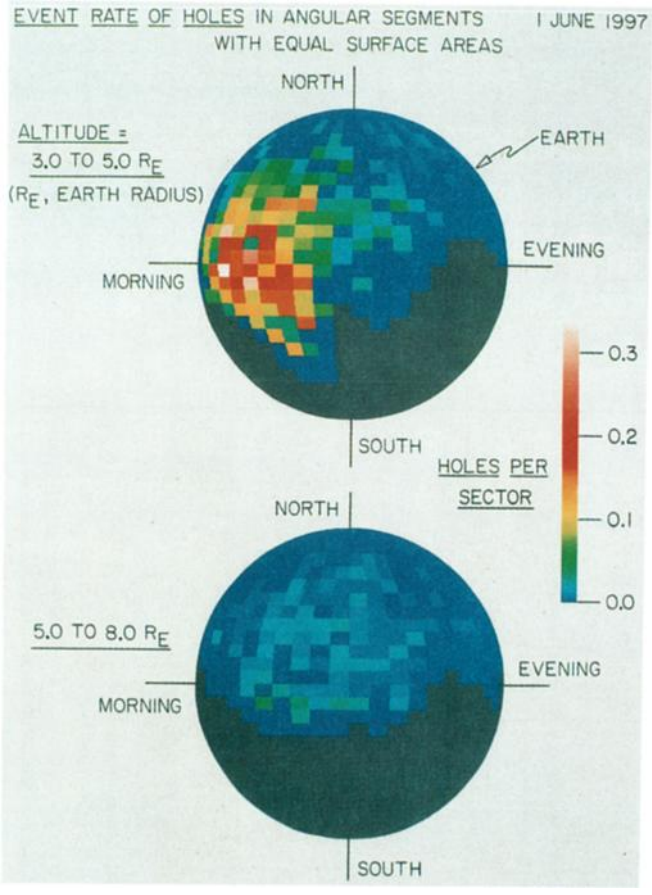

Plate 10. The occurrence rates for the number of atmospheric holes per sector for each Earth Camera image on June 1, 1997, in the same format as Plates 8 and 9. The holes per sector is more meaningful because the artifact hypothesis has been discarded as inconsistent with the data. Note the large decrease in hole frequency for the higher altitude bin. A pronounced local-time variation remains evident in the pixel maps of the dayside atmosphere.

northern hemisphere at altitudes of 4 to 8 R_E with the Earth Camera on the Polar spacecraft are shown in the upper panel of Figure 18. This altitude range is above that of the radiation zones. These rates are determined for the same months as for the Dynamics Explorer 1 measurements but 16 years later. A severe solar proton event precluded observations during November 6–7. The occurrence rates are also 2-day averages for the entire dayglow region viewed by the Earth Camera. The criteria for identification of the atmospheric holes remain the same as that for all of the results presented here. The only difference is the operation of the companion Low-Resolution Visible Camera during these winter months. This camera was activated on October 28, 1997, and increases the electronic noise in the Earth Camera such that the hole detection rate decreases by a factor of 3.2 (±0.3). This is a well-determined decrease during the period October 26 through November 1 for which the atmospheric hole rate is constant. With the exception of this turn-on of the visible camera there is no other significant operating change for the Earth Camera for the observations reported in this paper.

Examination of the atmospheric hole rates as determined with the Earth Camera in the upper panel of Figure 18 reveals the exciting result that the features are qualitatively similar to those found in the Dynamics Explorer 1 data within the statistical accuracy of the two data sets. That is, these features are the maximum intensities in early November, the brief plateau in mid-November, the decrease to a plateau spanning late November to mid-December, the further decrease to a plateau during the period mid-December through early January, and the notable minimum of intensities during mid-January with subsequent recovery. The Dynamics Explorer 1 observations are shown in the bottom panel of Figure 18. Averages for the rate plateaus are indicated in Figure 18. It is remarkable that two different spacecraft with entirely different instruments and in different polar orbits should determine strikingly similar seasonal variations during periods separated by 16 years.

A line summary of the observations of atmospheric hole rates with the Polar and the Dynamics Explorer 1 spacecraft, and the forward scatter radar rates with the Canadian radar, are shown in Figure 19 in order to facilitate the comparison of the three series of measurements. These observations span a period of 42 years and indi-

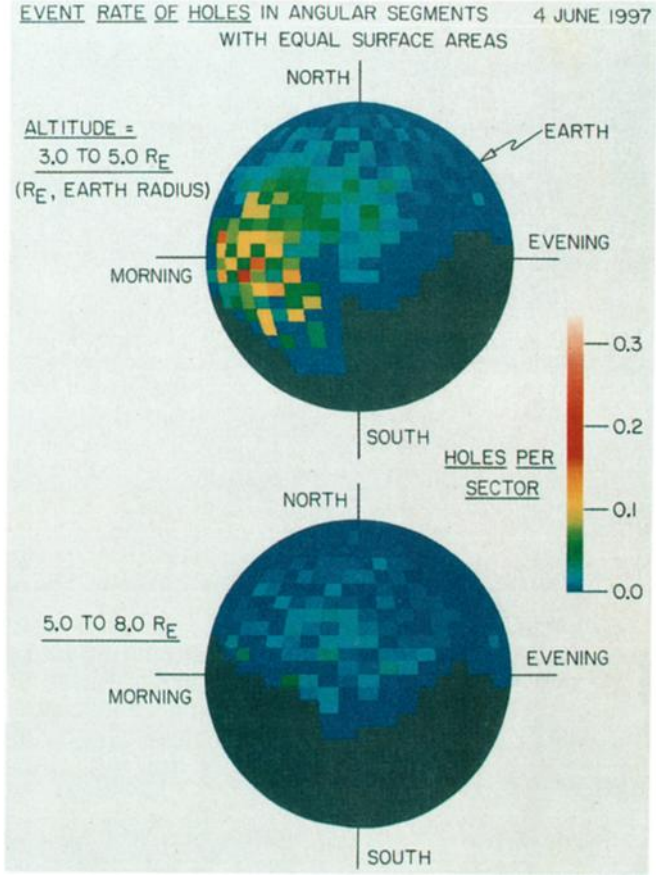

Plate 11. Continuation of Plate 10 for June 4, 1997.

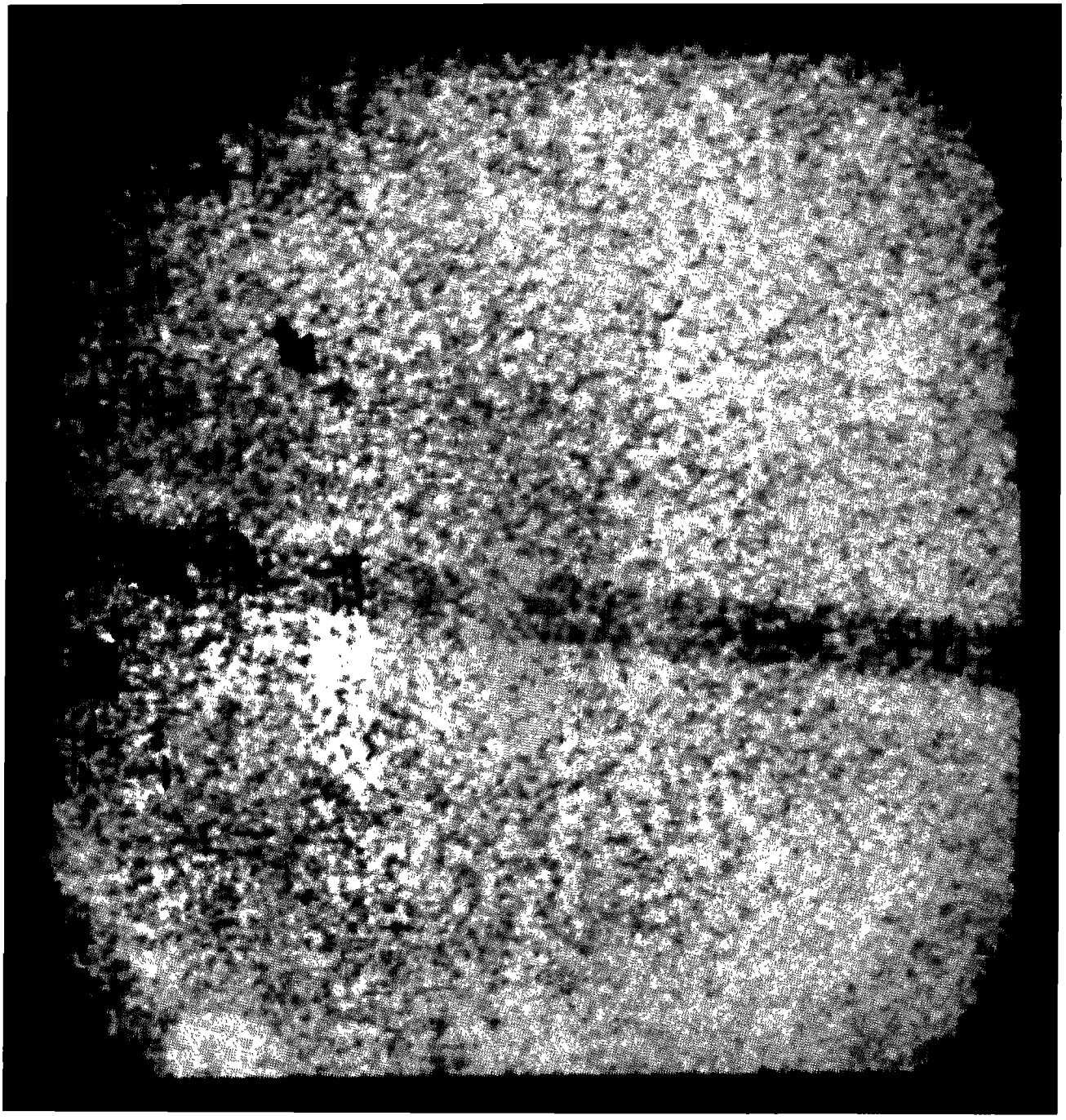

Plate 12. Sighting of an atmospheric hole when the spacecraft is at very low altitudes. The number of pixels is large and the diameter of the hole is about 100 km. This sighting corresponds to the viewing shown in the bottom panel of Figure 15. This image was taken at 0303:18 UT on April 23, 1997, at a spacecraft altitude, latitude and longitude of 7621 km, −40.2°N and 122.6°E, respectively.

Plate 13. Pixel map for the large atmospheric hole seen in the image in Plate 12. Pixels with decreases in responses ≤ 0.0 σ to −3.0 σ are coded with colors different than the background yellow which corresponds to higher pixel responses. Brown corresponds to the darkest pixels. The atmospheric hole consists of a cluster of about 50 darkened pixels.

Plate 14. Continuation of Plate 13 for another example of a large atmospheric hole observed when the spacecraft was located at low altitudes with the color bar extending from −0.5 σ to −3.0 σ. This pixel map was taken at 0222:20 UT on April 26, 1997, when the spacecraft altitude, latitude and longitude were 13,005 km, −1.9°N and 132.8°E, respectively.

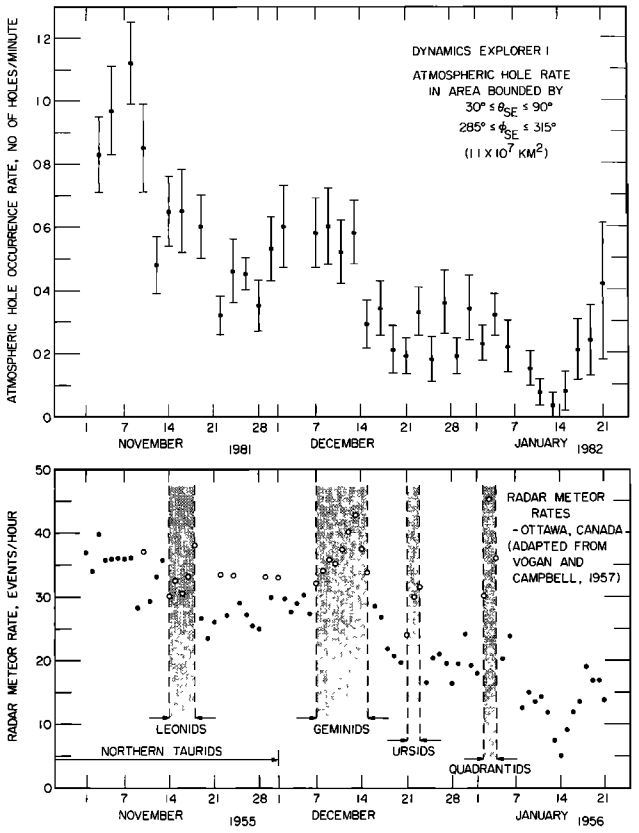

Figure 17. (top) Average occurrence rates of atmospheric holes during the period November 1981 through late January 1982 as observed with Dynamics Explorer 1. (bottom) Forward scatter meteor rates reported by *Vogan and Campbell* [1957] for the same months but for earlier years 1955 and 1956 [after *Frank and Sigwarth,* 1993].

cate that the phenomenon is not transient on this time scale.

5. Summary and Discussion

An extensive study of the images taken with the Earth Camera on the Polar spacecraft is reported for the phenomenon of atmospheric holes. These analyses were first directed toward a comprehensive examination of all currently suggested artifacts which might give rise to the transient clusters of darkened pixels which are called atmospheric holes. The selection criteria which are used to evaluate the geophysical effects exhibited by the atmospheric holes were shown to provide robust protection from the aliasing by instrumental artifacts. Our summary and discussion provide an overview of the various findings reported in this paper.

An automated survey of the images for the purposes of the identification of the atmospheric holes was employed in order to avoid any selectivity by a visual search method. The criteria for the automated survey were simple and straightforward. An atmospheric hole was required to have five or more contiguous pixels, each with intensities which were lower than the local mean value by −2.5 σ or more. The standard deviation was required to be ≥ 7.5 DN (digitization numbers for the pixel responses) in order to eliminate false detections of holes due to energetic charged particles in the radiation zones. The local mean and standard deviation for each pixel in an image were determined by placing a 7 × 7 pixel block centered on the pixel in question and using the 32 peripheral pixels for the computations. The only correction to the images was the reduction of the effects of charge deposition in the sensor by penetrating charged particles. This procedure was also simple in that it identified pixels with responses greater than 30 DN above the mean of the 7 × 7 pixel block and replaced these values with the mean values. Although this procedure was applied for all the images it was important only for a small range of spacecraft altitudes in the radiation zones in the 1–R_E altitude bin centered at 3 R_E for approximately 10 to 25 min during the 17.6-hour orbital period of the spacecraft.

Important aspects of the investigation of instrumental effects are as follows.

1. The period in mid-January during which no atmospheric holes were detected provided an excellent opportunity to have a very effective calibration series of

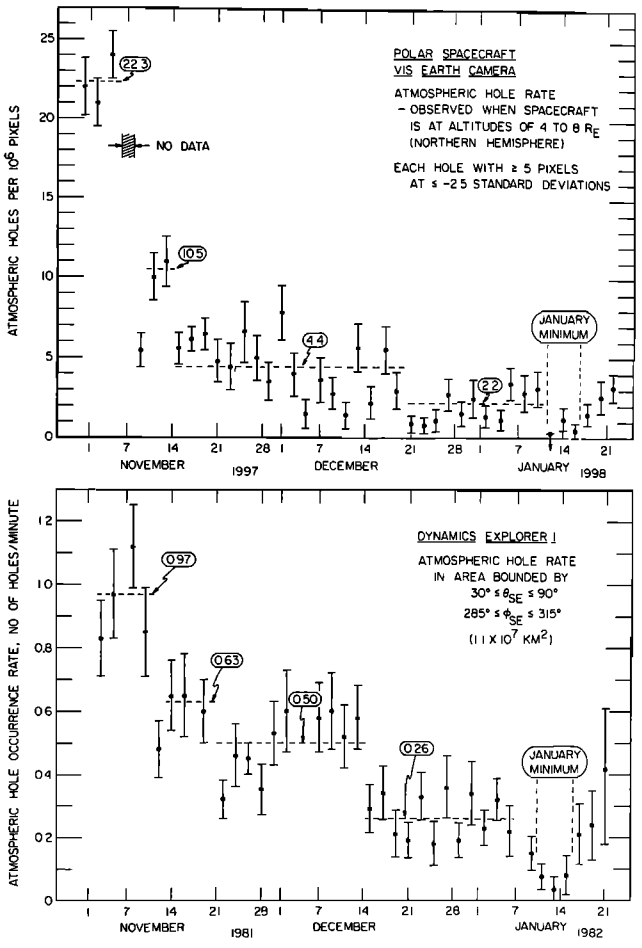

Figure 18. (top) Occurrence rates of atmospheric holes as observed by the Earth Camera on the Polar spacecraft during the period November 1997 through late January 1998. (bottom) Atmospheric hole rates as observed with Dynamics Explorer 1 during the same months but for different years, 1981 and 1982.

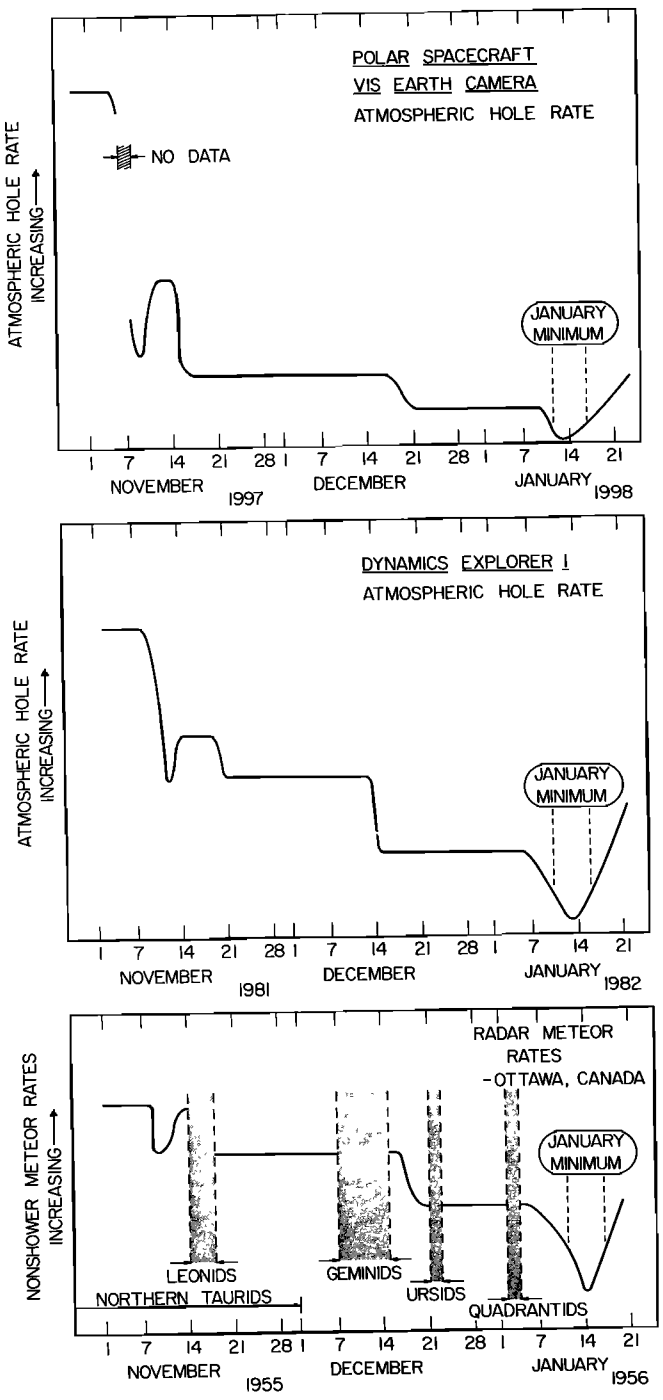

Figure 19. Line summary of the atmospheric hole rates observed (top) with the Polar spacecraft and (middle) with the Dynamics Explorer 1 spacecraft and (bottom) meteor rates with the Canadian forward scatter radar. Ordinates are proportional to those shown in Figures 17 and 18.

images which were equivalent to an extensive postlaunch laboratory calibration. These inflight calibration images were extremely important in establishing the instrument noise performance without the presence of atmospheric holes and with the actual temperatures and operating voltages for the instrument. These images verify the accuracy of our computations of random hole rates.

2. The criterion for pixel darkening by response decreases of $\leq -2.5\ \sigma$ was shown to provide random rates which were considerably lesser than the observed hole rates, except during the above mid-January calibration period. On the other hand, a weaker criterion of $\leq -2.0\ \sigma$ allows random rates which are significantly lesser than the observed rates at the higher spacecraft altitudes but also allows a significant fraction of false hole detections due to such instrumental effects as penetrating radiation and sensor hot spots.

3. The immunity of the selection criteria to false detections due to the large fluxes of penetrating electrons in the outer radiation zone was tested by comparing the simultaneous occurrence rates of atmospheric holes and the fluxes of energetic electrons as determined with the onboard HIST charged particle instrument. No obvious correlation of these two measurements was found for spin-averaged electron (2.7 MeV) intensities $\lesssim 2 \times 10^4 (\mathrm{cm}^{-2}\ \mathrm{s}\ \mathrm{sr}\ \mathrm{MeV})^{-1}$. At higher intensities the automated search algorithm recorded a substantial number of false identifications. No images taken at these higher electron intensities were used for the automated search for geophysical effects as reported here.

4. The variations of sensitivity of the CCD in the sensor of the Earth Camera can provide "hot spots" for which the probability for the recording of darkened clusters is greater. The atmospheric holes are expected to be randomly distributed over the area of the sensor. Our selection criteria limits these effects to about 3% of the total number of hole events, an acceptable number. On the other hand, if the criteria are relaxed to $\leq -2.0\ \sigma$ the hot spots provide an unacceptable number of such events.

5. The near-ultraviolet response of the sensor of the Earth Camera is sufficient that high-altitude clouds are recorded in the images. The relevant wavelength range is 200 to 300 nm. A sufficiently large near-ultraviolet response would preclude detection of atmospheric holes because of the large background. For viewing when the spacecraft is at equatorial latitudes the additional signal due to the clouds is about 40%. As the spacecraft latitude increases this contribution also decreases due to the increased path length for the reflected solar radiation to be seen at the spacecraft. The Low-Resolution Visible Camera of the VIS instrumentation is used to show that the contribution of near-ultraviolet radiation for the off-cloud areas is less than an acceptable 15% of the O I 130.4-nm signal. Since the high-altitude clouds typically cover only about 5 to 10% or less of a dayglow image the loss of area is acceptable. The positions of the atmospheric holes were not found to be correlated with cloud features. In addition the strong correlation of the seasonal variations as observed with the Polar and Dynamics Explorer 1 cameras further confirms that the Earth Camera images are not aliased by near-ultraviolet emissions because the Dynamics Explorer 1 camera was not sensitive to these long-wavelength radiations.

The above study which eliminates substantial instrumental effects for the criteria employed for the automated search provided the opportunity to establish the following geophysical effects.

1. The altitude dependence of the occurrence rates of atmospheric holes was firmly established with global maps of these rates in the Earth's atmosphere for two altitude buckets. The altitude dependence was also clearly shown by the decreases in event rates for a fixed area of the dayglow in 1-R_E bins as the spacecraft altitude increased. These decreases are simply due to the fact that lesser numbers of the holes can be detected by the Earth Camera with increasing altitude as the apparent sizes of the holes decrease beneath the spatial resolution of the camera.

2. It is notable that the typical global rates in the range of a few tens per minute for the atmospheric holes as reported here for the Polar Earth Camera are similar to the average global rates as observed with Dynamics Explorer 1 [*Frank and Sigwarth*, 1993]. The designs of these two cameras are entirely different, i.e., the Earth Camera is based upon CCD technology and the Dynamics Explorer 1 instrument was a simple spin-scan photometer. The thresholds for atmospheric hole detection were not arbitrary but were assigned at well-defined knees in the observed probability functions (see Figure 8). If the atmospheric holes were due to instrument artifacts, the occurrence rates would be expected to differ by large factors for the two cameras. The fact that the global rates are similar is strongly supportive of atmospheric holes as a geophysical reality.

3. A strong local-time dependence of the occurrence rates of atmospheric holes is observed in Earth's atmosphere. The occurrence rates favor local late-morning relative to local evening. The same local-time variation is seen at low and high altitudes. A similar local-time variation was previously observed with Dynamics Explorer 1.

4. At the very lowest altitudes in the range of 1 to 2 R_E the occurrence frequencies of atmospheric holes are significantly lesser than the rates observed at the higher altitude of 3 R_E. This effect is due to the fact that only a relatively small fraction of the dayglow area is viewed at the lower altitudes. Such a decrease in the frequency of atmospheric holes in the images can only be attributed to a distribution of real objects within the field of view of the Earth Camera.

5. The atmospheric hole size is shown to increase with decreasing altitude, as expected. At the lowest altitudes a 100-km-diameter atmospheric hole is expected to be a cluster of darkened pixels with larger pixel numbers relative to the high-altitude detections. For example, the pixel resolution of the Earth Camera is about 13 km when the spacecraft is at an altitude of 1.5 R_E. Clusters of 40 or 50 darkened pixels are expected and are found.

6. The seasonal variations of the occurrence rates of atmospheric holes as viewed with the Earth Camera have been determined for the period November 1, 1997, through late January 1998. These rates vary by a factor $\gtrsim$ 10 during this period. These variations are characterized by large intensities during early November, a brief plateau of lesser intensities during mid-November, an extended period of lesser and more or less constant intensities for late November through mid-December, a decrease to a lesser plateau of intensities from mid-December to early January, and a well-defined minimum in mid-January with subsequent recovery. Remarkably, this is the same signature observed with Dynamics Explorer 1 during the same months 16 years earlier and in the nonshower forward scatter meteor rates observed in Ottawa, Canada, some 42 years earlier than the present Polar spacecraft observations.

The sources of instrumental effects for detection of atmospheric holes with the Earth Camera on board the Polar spacecraft have been comprehensively investigated. The automated determination of the strong geophysical effects reported in this paper validates the reality of the atmospheric holes.

Acknowledgments. The authors are grateful to J. B. Blake and R. S. Selesnick of The Aerospace Corporation for the measurements of energetic electrons with their HIST instrumentation on the Polar spacecraft and to R. A. Mewaldt of the California Institute of Technology for the energetic electron measurements with the PET instrumentation of the SAMPEX satellite. This research was supported in part at the University of Iowa by NASA contract NAS5-30316.

Janet G. Luhmann thanks R. Gladstone and another referee for their assistance in evaluating this paper.

References

Blake, J. B., et al., CEPPAD: Comprehensive Energetic Particle and Pitch Angle Distribution Experiment on POLAR, *Space Sci. Rev., 71*, 531–562, 1995.

Cook, W. R., et al., PET: A proton/electron telescope for studies of magnetospheric, solar, and galactic particles, *IEEE Trans. Geosc. Remote Sens., 31*, 565–571, 1993.

Cragin, B. L., W. B. Hanson, R. R. Hodges, and D. Zuccaro, Comment on the papers "On the influx of small comets into the Earth's upper atmosphere, I. Observations and II. Interpretation," *Geophys. Res. Lett., 14*, 573–576, 1987.

Craven, J. D., A. C. Nicholas, L. A. Frank, D. J. Strickland, and T. J. Immel, Variations in the FUV dayglow after intense auroral activity, *Geophys. Res. Lett., 21*, 2783–2796, 1994.

Dessler, A. J., The small comet hypothesis, *Rev. Geophys., 29*, 355–382, 1991.

Frank, L. A., J. D. Craven, K. L. Ackerson, M. R. English, R. H. Eather, and R. L. Carovillano, Global auroral imaging instrumentation for the Dynamics Explorer mission, *Space Sci. Instrum., 5*, 369–393, 1981.

Frank, L. A., J. B. Sigwarth, and J. D. Craven, On the influx of small comets into the Earth's upper atmosphere, I, Observations, *Geophys. Res. Lett., 13*, 303–306, 1986a.

Frank, L. A., J. B. Sigwarth, and J. D. Craven, On the influx of small comets into the Earth's upper atmosphere, II, Interpretation, *Geophys. Res. Lett., 13*, 307–310, 1986b.

Frank, L. A., J. B. Sigwarth, and J. D. Craven, Reply to Soter, *Geophys. Res. Lett., 14*, 164–167, 1987.

Frank, L. A., and J. B. Sigwarth, Atmospheric holes and small comets, *Rev. Geophys., 31*, 1–28, 1993.

Frank, L. A., J. B. Sigwarth, J. D. Craven, J. P. Cravens, J. S. Dolan, M. R. Dvorsky, P. K. Hardebeck, J. D. Harvey, and D. Muller, The visible imaging system (VIS) for the Polar spacecraft, *Space Sci. Rev., 71*, 297–328, 1995.

Frank, L. A., and J. B. Sigwarth, Transient decreases of Earth's far-ultraviolet dayglow, *Geophys. Res. Lett., 24*, 2423–2426, 1997a.

Frank, L. A., and J. B. Sigwarth, Simultaneous observations of transient decreases of Earth's far-ultraviolet dayglow with two cameras, *Geophys. Res. Lett., 24*, 2427–2430, 1997b.

Frank, L. A., and J. B. Sigwarth, Detection of atomic oxygen trails of small comets in the vicinity of Earth, *Geophys. Res. Lett., 24*, 2431–2434, 1997c.

Frank, L. A., and J. B. Sigwarth, Trails of OH emissions from small comets near Earth, *Geophys. Res. Lett., 24*, 2435–2438, 1997d.

Gladstone, G. R., Simulations of DE 1 UV airglow images, *J. Geophys. Res.*, *99*, 11,411–11,448, 1994.

McFadden, J. P., F. S. Mozer, J. Vernetti, and I. Sircar, An instrumental source for the dark pixel clusters in the Polar VIS and UVI experiments, *Geophys. Res. Lett.*, *25*, 3705–3708, 1998.

McKinley, D. W. R., *Meteor Science and Engineering*, McGraw–Hill, New York, 1961.

Meier, R. R., R. Cox, D. J. Strickland, J. D. Craven, and L. A. Frank, Interpretation of Dynamics Explorer far UV images of the quiet time thermosphere, *J. Geophys. Res.*, *100*, 5777–5794, 1995.

Mozer, F. S., J. P. McFadden, I. Sircar, and J. Vernetti, Small comet "atmospheric holes" are instrument noise, *Geophys. Res. Lett.*, *25*, 3713–3716, 1998.

Parks, G., M. Brittnacher, L. J. Chen, R. Elsen, M. McCarthy, G. Germany, and J. Spann, Does the UVI on Polar detect cosmic snowballs?, *Geophys. Res. Lett.*, *24*, 3109–3112, 1997.

Parks, G., M. Brittnacher, R. Elsen, M. McCarthy, J. M. O'Meara, G. Germany, and J. Spann, Comparison of dark pixels observed by VIS and UVI in dayglow images, *Geophys. Res. Lett.*, *25*, 3063–3066, 1998.

Torr, M. R., et al., A far ultraviolet imager for the International Solar-Terrestrial Physics Mission, *Space Sci. Rev.*, *71*, 329–383, 1995.

Vogan, E. L., and L. L. Campbell, Meteor signal rates observed in forward-scatter, *Can. J. Phys.*, *35*, 1176–1189, 1957.

L. A. Frank and J. B. Sigwarth, Department of Physics and Astronomy, University of Iowa, Iowa City, IA 52242–1479. (louis-frank@uiowa.edu)

(Received January 12, 1998; revised August 31, 1998; accepted August 31, 1998.)